Applied Energy 254 (2019) 113646

Contents lists available at ScienceDirect

Applied Energy

journal homepage: www.elsevier.com/locate/apenergy

Thermal energy storage (TES) with phase change materials (PCM) in solar power plants (CSP). Concept and plant performance

Cristina Prieto[a,*], Luisa F. Cabeza[b]

[a] Abengoa, Energía Solar 1, 41014 Sevilla, Spain
[b] GREiA Research Group, INSPIRES Research Centre, Universitat de Lleida, Pere de Cabrera s/n, 25001 Lleida, Spain

HIGHLIGHTS

- Cascade PCM as potential low cost and high energy TES systems.
- Daily, monthly, and annual transient model of the plant performance with cascade PCM.
- Similarity of PCM and double tank storage system in CSP.

ARTICLE INFO

Keywords:
Thermal energy storage (TES)
Concentrated solar power (CSP)
Phase change material (PCM)
Cascade system
Transient simulation
Plant performance

ABSTRACT

Concentrated solar power (CSP) is today recognized as a unique renewable energy for electricity generation due to its capability to provide dispatchable electricity incorporating thermal energy storage (TES). Molten salts TES is the most widespread technology in commercial CSP but the industry is looking for cheaper and more efficient TES systems and phase change materials (PCM) have been highlighted as potential low cost and high energy TES systems. This paper presents a completely new concept of PCM energy storage systems to be used in solar thermal electricity plants with its technical assessment. A cascade type PCM storage system is evaluated, using four buckets with the PCM organized based on melting temperature and the latent energy of the materials. Daily, monthly, and annual transient simulations of the plant performance are carried out. The main conclusion is the similarity between this new concept and the commercial two-tank indirect molten salt system. The cumulative power production over the year is similar and the net production of both systems is well matched.

1. Introduction

Today it is well recognised that concentrated solar power (CSP) is a unique renewable energy for electricity generation due to its capability to provide dispachable electricity [1]. To do so, CSP plants incorporate thermal energy storage (TES). Molten salts TES is the most widespread technology in commercial CSP, and can be included with both parabolic trough and with tower, the two commercial CSP technologies today in the market. Molten salts TES is used as indirect storage system with the ability to discharge at constant conditions, maintaining high cycle efficiency.

But looking for cheaper and more efficient TES systems, CSP industry as looked at thermochemical TES [2] and also at latent TES with phase change materials (PCM). Past research has highlighted the potential low cost and high energy density of PCM TES systems. Specifically, by utilizing the latent heat of phase change instead of just the sensible heat capacity of the storage material, potentially lower capital costs then two tank molten salt systems have been calculated [3,4].

PCM storage was mainly studied with two different concepts, with shell and tubes heat exchanges with PCM working at high enough temperatures to be used in CSP, or with packed bed storage tanks with the PCM encapsulated usually in balls [5,6]. Due to the low thermal conductivity of PCM, Belusko et al. [7,8] studied the impact of the tube configuration on the discharge effectiveness and on the design of the heat exchanger. Similarly, Abujas et al. [9] studied a new fin design to increase the performance of such PCM tanks, and Kumar and Saha [10] the use of a high porosity metal matrix.

Packed bed PCM tanks at high temperature with the idea of thermocline TES was numerically studied by Galione et al. [11], showing it as an alternative to molten salts TES. A similar study was carried out by Abdulla and Redhy [12], comparing it to a one-tank system, showing better performance with packed bed PCM is used. Recently, Elfeky et al. [13] performed a theoretical study of the use of packed bed PCM in a cascade system. The use of PCM in cascade was theoretically already

* Corresponding author.
E-mail address: cristina.prieto@abengoa.com (C. Prieto).

https://doi.org/10.1016/j.apenergy.2019.113646
Received 2 January 2019; Received in revised form 9 July 2019; Accepted 1 August 2019
Available online 13 August 2019
0306-2619/

presented in 1999 [14]. As stated by Peiró et al. [15], there are multiple advantages of the use of this PCM configuration:

- Increase in the heat transfer rate during charge and discharge, especially during the phase change.
- Uniform and lower outlet heat transfer fluid (HTF) temperature of a longer period during charge and discharge.
- Faster charge and discharge processes.
- Increase of exergy efficiency.

Tehrani et al. [16] compared using a shell and tube heat exchanger in a cascade PCM system with the already known concrete storage system. Their system incorporated a cascade system with sensible-latent-sensible storage similar to that already presented by Tamme et al. [4], who used different sensible storage tanks in cascade to increase the performance of the overall plant, and by Laing et al. [17], who used a system with sensible-latent-sensible storage for direct steam generation power plants. In this paper, a new cascade PCM storage system for better performance of CSP plants is presented and evaluated. The concept is new from different points of view: the application of the cascade concept in CSP with only PCM, the arrangement of the PCM cascade tanks, and the arrangement of the PCM inside the tanks; moreover, this paper is the first time to compare such new storage concept with the commercial molten salt system. The economic evaluation of such concept is presented in Part 2 of this study [18].

2. Storage concept

The phase change material (PCM) thermal energy storage (TES) considered in this study utilizes the latent energy change of materials to store thermal energy generated by the solar field in a concentrated solar thermal power plant. It does this using an array of materials organized based on melting temperature. Similar to other forms of TES, the heat transfer fluid (HTF) runs through a heat exchanger where its energy is extracted. Then, during discharge, the same energy is recaptured as the storage material solidifies.

PCM storage operates in a fully passive manner, that is, the storage material is stationary during charge and discharge. The HTF is pumped through a tube registry embedded in the PCM that facilitates heat transfer into the PCM. These tube registries currently are assumed to be small vertically oriented heat exchangers organized into groups in series and in parallel. Fig. 1 shows a cutaway view of one such heat exchanger. The tan coloured PCM is sandwiched between the HTF pipes in such spacing as to allow the proper amount of heat transfer.

Many heat exchangers are then arrayed in both parallel and series in order to achieve the correct flow rates, outlet temperatures and overall performance. The number in series is based on the required effective tube length and the number in parallel is based on the required effective tube number. To meet the required outlet temperatures multiple PCMs must be arrayed in order of melting temperature to step the HTF temperature to the proper level. Each PCM with a unique melting temperature is grouped into an individual bucket. These buckets are then arrayed in series and collectively referred to as a cascade.

Fig. 2 shows a typical PCM storage system in both charge and discharge. Because the enthalpy of fusions, and pinch point temperatures are different for each bucket, each bucket has a different number of heat exchangers.

The system dimensions are largely governed by the thermal properties of the individual PCMs and the pinch points of the individual buckets during charge and discharge. This is compounded by the transient nature of the PCM freezing and melting on the tube surfaces. Overall this causes the system to be hard to size correctly without iteration. Instead the system is sized iteratively to achieve as stable an outlet temperature as possible at the correct outlet temperature and storage size.

Phase change materials were selected from those available in the literature [19]. Fig. 3 shows the cost per kJ of capacity of the materials considered; those with the lower cost were selected. Their technical description is presented in Table 1.

3. Modelling

In order to address the behaviour of the cascade PCM storage system in a CSP plant a performance model was developed. This model is able to simulate the transient performance of the PCM storage system integrated into a power plant model. Together with component models for all other components in a full scale CSP plant, the PCM model is able to estimate storage performance during a representative operation based on typical ambient conditions and solar radiation.

3.1. PCM modelling

The development of the TES component is of most relevance to the assessment of PCM TES technology. In order to be integrated with a

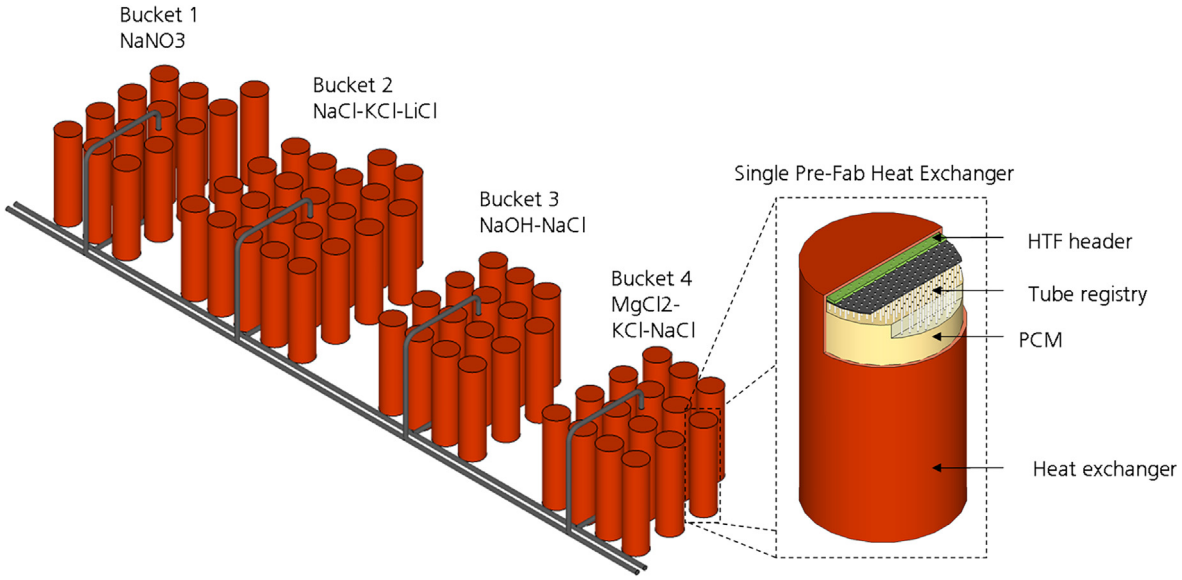

Fig. 1. Depiction of the entire PCM cascade and a single pre-fabricated heat exchanger.

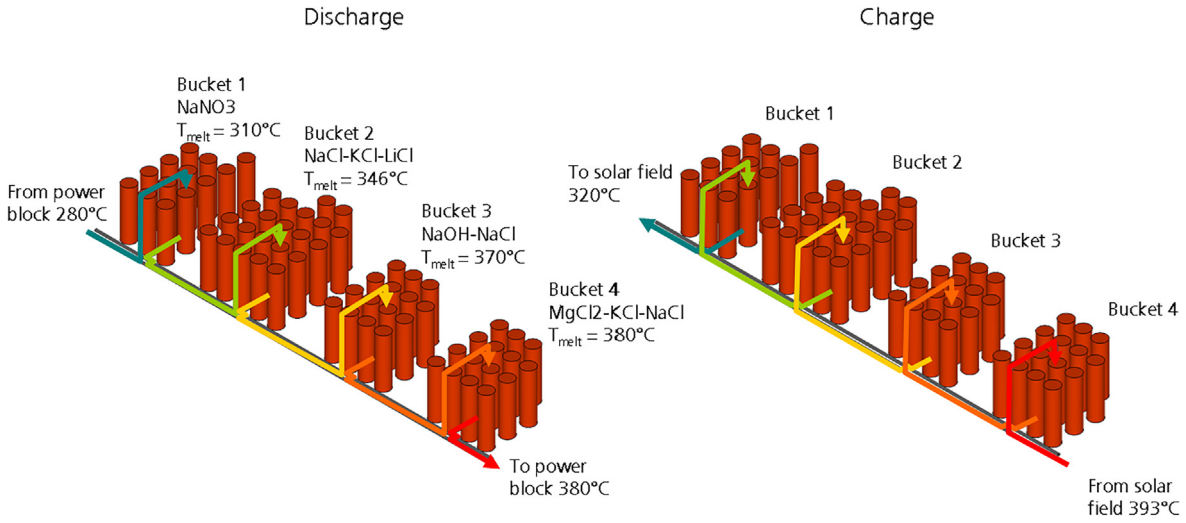

Fig. 2. Charging and discharging orientations of a PCM system comprised of pre-fabricated heat exchangers.

realistic plant model, the component had to model both sensible and latent heat storage for any amount of partial charge and discharge cycles. This was accomplished by the creation of a two dimensional implicit model based on an adaptive Crank-Nicolson or Backwards Euler grid.

This model includes several key assumptions to strike a compromise between accuracy, complexity and runtime. The major assumptions made are:

No axial conduction.
One node per phase group (phase group is defined in the next section).
Metastable tolerance of 1 °C.
Total phase change complete when mass original phase is less than 1% mass of original 100% solid PCM node mass.
Use of friction factor-based Nusselt number correlations.
Constant thermophysical properties.
No volume change during melting or freezing.
System properties in coefficients are based on the previous time step.
Some thermal properties of mixtures are calculated as the molar average of their constituents.
Constant exterior tank surface temperature.

The goal of the model is to solve for the temperature at specific axial and radial locations in a system containing a metal tube filled with a heat transfer fluid (HTF) surrounded by a latent storage material. Fig. 4 shows the system being solved at a representative time step. As time progresses, the number of phase groups may change but the number of axial sections remains constant. Nine different node types are present in

Table 1
Technical description of materials used in the system [19]

	Bucket 1	Bucket 2	Bucket 3	Bucket 4
Chemical (mass %)	$NaNO_3$	NaCl (33%) KCl (24%) LiCl (43%)	NaOH (80%) NaCl (20%)	$MgCl_2$ (60%) KCl (20.4%) NaCl (19.6%)
Melting point (°C)	310	346	370	380
Melting enthalpy (kJ/kg)	172	280	370	400
Thermal conductivity liquid (W/m·K)	0.56	0.68	0.87	1.08
Thermal conductivity solid (W/m·K)	0.56	2.65	2.35	2.29
Solid density (kg/m^3)	1929	1897	2104	2055
Liquid density (kg/m^3)	1882	1512	1743	1609
Specific heat (kJ/kg·K)	1.82	1.34	2.01	1.04
Kinematic viscosity (m^2/2)	1.51E−06	7.94E−07	1.92E−06	9.63E−07
Volumetric expansion (%)	2.5%	25.5%	20.7%	27.7%
Mass in system (kg)	3,122,644	7,292,907	6,527,257	3,747,172

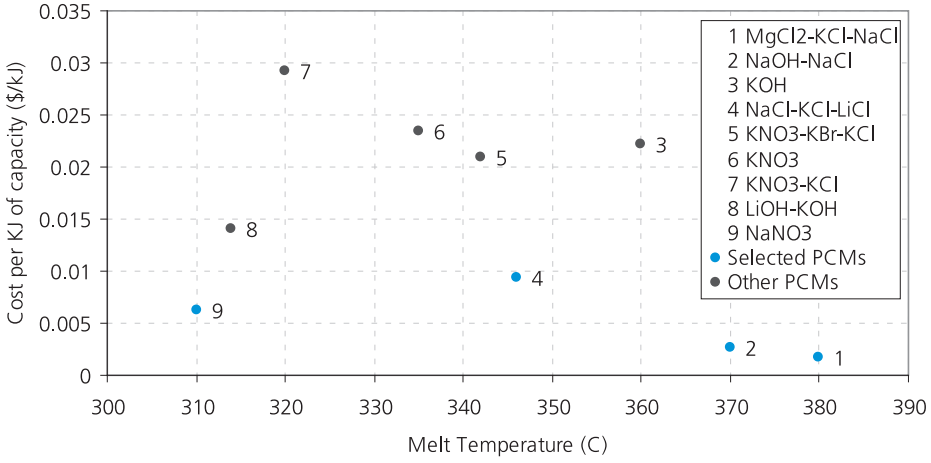

Fig. 3. Cost per kJ of each PCM considered.

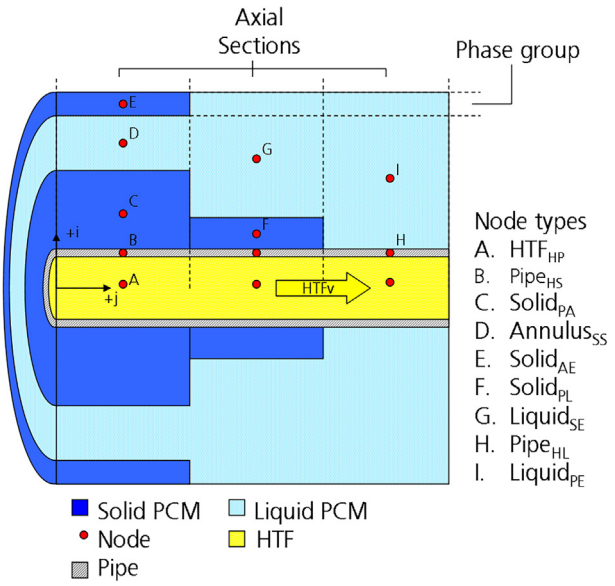

Fig. 4. An example of the transient system at a representative time step.

the figure; however, this is not an exhaustive list of the different types of nodes used by this component, it is just a simplification for clarity.

A complete and detailed description of each node type and equation in the model is described next. Each node type is defined by its own material and the material of the surrounding nodes. For example, a node that is solid PCM that has the pipe on one side and a liquid node on the other would be written as Solid$_{PL}$. If, however, the liquid node had solid on the other side, then we would write the node type as Solid$_{PA}$ because the liquid node is an annulus liquid node. Using the Crank Nicolson approximation:

- Solid PCM node with pipe on the interior edge and an annulus of liquid on the outer edge (Solid$_{PA}$):

$$T_{Si,j}^{n+1} = T_{Si,j}^{n} + \frac{\Delta t}{2m_{Si,j}C_S}\left[\frac{1}{R_{PS}}(T_{Pi-1,j}^{n+1} - T_{Si,j}^{n+1}) - \frac{1}{R_{SA}}(T_{Si,j}^{n+1} - T_{Ai+1,j}^{n+1})\right] + \frac{\Delta t}{2m_{Si,j}C_S}\left[\frac{1}{R_{PS}}(T_{Pi-1,j}^{n} - T_{Si,j}^{n}) - \frac{1}{R_{SA}}(T_{Si,j}^{n} - T_{Ai+1,j}^{n})\right]$$

- Solid PCM node with a liquid annulus on the inner edge and a liquid annulus on the out edge (Solid$_{AA}$):

$$T_{Si,j}^{n+1} = T_{Si,j}^{n} + \frac{\Delta t}{2m_{Si,j}C_S}\left[\frac{1}{R_{AS}}(T_{Ai-1,j}^{n+1} - T_{Si,j}^{n+1}) - \frac{1}{R_{SA}}(T_{Si,j}^{n+1} - T_{Ai+1,j}^{n+1})\right] + \frac{\Delta t}{2m_{Si,j}C_S}\left[\frac{1}{R_{AS}}(T_{Ai-1,j}^{n} - T_{Si,j}^{n}) - \frac{1}{R_{SA}}(T_{Si,j}^{n} - T_{Ai+1,j}^{n})\right]$$

- Solid PCM node with a liquid annulus on the inner edge and a liquid node on the outer edge that extends to the adiabatic boundary (Solid$_{AL}$):

$$T_{Si,j}^{n+1} = T_{Si,j}^{n} + \frac{\Delta t}{2m_{Si,j}C_S}\left[\frac{1}{R_{AS}}(T_{Ai-1,j}^{n+1} - T_{Si,j}^{n+1}) - \frac{1}{R_{SL}}(T_{Si,j}^{n+1} - T_{Li+1,j}^{n+1})\right] + \frac{\Delta t}{2m_{Si,j}C_S}\left[\frac{1}{R_{AS}}(T_{Ai-1,j}^{n} - T_{Si,j}^{n}) - \frac{1}{R_{SL}}(T_{Si,j}^{n} - T_{Li+1,j}^{n})\right]$$

- Solid PCM node with a pipe on the inner edge and a liquid node on the outer edge that extends to the adiabatic boundary (Solid$_{PL}$):

$$T_{Si,j}^{n+1} = T_{Si,j}^{n} + \frac{\Delta t}{2m_{Si,j}C_S}\left[\frac{1}{R_{PS}}(T_{Pi-1,j}^{n+1} - T_{Si,j}^{n+1}) - \frac{1}{R_{SL}}(T_{Si,j}^{n+1} - T_{Li+1,j}^{n+1})\right] + \frac{\Delta t}{2m_{Si,j}C_S}\left[\frac{1}{R_{PS}}(T_{Pi-1,j}^{n} - T_{Si,j}^{n}) - \frac{1}{R_{SL}}(T_{Si,j}^{n} - T_{Li+1,j}^{n})\right]$$

- Solid PCM node with a liquid annulus on the inner edge and the boundary on its outer edge (Solid$_{AE}$):

$$T_{Si,j}^{n+1} = T_{Si,j}^{n} + \frac{\Delta t}{2m_{Si,j}C_S}\left[\frac{1}{R_{AS}}(T_{Ai-1,j}^{n+1} - T_{Si,j}^{n+1}) - \dot{Q}_{loss}\right] + \frac{\Delta t}{2m_{Si,j}C_S}\left[\frac{1}{R_{AS}}(T_{Ai-1,j}^{n} - T_{Si,j}^{n}) - \dot{Q}_{loss}\right]$$

- Solid PCM node with a pipe on its inner edge and the boundary on its outer edge (Solid$_{PE}$):

$$T_{Si,j}^{n+1} = T_{Si,j}^{n} + \frac{\Delta t}{2m_{Si,j}C_S}\left[\frac{1}{R_{PS}}(T_{Pi-1,j}^{n+1} - T_{Si,j}^{n+1}) - \dot{Q}_{loss}\right] + \frac{\Delta t}{2m_{Si,j}C_S}\left[\frac{1}{R_{AS}}(T_{Ai-1,j}^{n} - T_{Si,j}^{n}) - \dot{Q}_{loss}\right]$$

- Liquid PCM node with pipe on its inner boundary and the boundary on its outer edge (Liquid$_{PE}$):

$$T_{Li,j}^{n+1} = T_{Li,j}^{n} + \frac{\Delta t}{2m_{Li,j}C_L}\left[\frac{1}{R_{PL}}(T_{Pi-1,j}^{n+1} - T_{Li,j}^{n+1}) - \dot{Q}_{loss}\right] + \frac{\Delta t}{2m_{Li,j}C_L}\left[\frac{1}{R_{PL}}(T_{Pi-1,j}^{n} - T_{Li,j}^{n}) - \dot{Q}_{loss}\right]$$

- Liquid PCM node with a solid node on its inner boundary and the boundary on its outer edge (Liquid$_{SE}$):

$$T_{Li,j}^{n+1} = T_{Li,j}^{n} + \frac{\Delta t}{2m_{Li,j}C_L}\left[\frac{1}{R_{SL}}(T_{Si-1,j}^{n+1} - T_{Li,j}^{n+1}) - \dot{Q}_{loss}\right] + \frac{\Delta t}{2m_{Li,j}C_L}\left[\frac{1}{R_{PL}}(T_{Pi-1,j}^{n} - T_{Li,j}^{n}) - \dot{Q}_{loss}\right]$$

- Annulus PCM node with the pipe on its inner edge and a solid node on its outer edge (Annulus$_{PS}$):

$$T_{Ai,j}^{n+1} = T_{Ai,j}^{n} + \frac{\Delta t}{2m_{Ai,j}C_L}\left[\frac{1}{R_{PA}}(T_{Pi-1,j}^{n+1} - T_{Ai,j}^{n+1}) - \frac{1}{R_{AS}}(T_{Ai,j}^{n+1} - T_{Si+1,j}^{n+1})\right] + \frac{\Delta t}{2m_{Ai,j}C_L}\left[\frac{1}{R_{PA}}(T_{Pi-1,j}^{n} - T_{Ai,j}^{n}) - \frac{1}{R_{AS}}(T_{Ai,j}^{n} - T_{Si+1,j}^{n})\right]$$

- Annulus PCM node with a solid node on its inner edge and a solid node on its outer edge (Annulus$_{SS}$):

$$T_{Ai,j}^{n+1} = T_{Ai,j}^{n} + \frac{\Delta t}{2m_{Ai,j}C_L}\left[\frac{1}{R_{SA}}(T_{Si-1,j}^{n+1} - T_{Ai,j}^{n+1}) - \frac{1}{R_{AS}}(T_{Ai,j}^{n+1} - T_{Si+1,j}^{n+1})\right] + \frac{\Delta t}{2m_{Ai,j}C_L}\left[\frac{1}{R_{SA}}(T_{Si-1,j}^{n} - T_{Ai,j}^{n}) - \frac{1}{R_{AS}}(T_{Ai,j}^{n} - T_{Si+1,j}^{n})\right]$$

- HTF node with pipe on its outer edge (HTF_{HP}):

$$T_{Hi,j}^{n+1} = T_{Hi,j}^{n} + \frac{\Delta t}{2m_{HTFi,j}C_H}\left[\dot{m}_{HTF}C_H(T_{Hi,j-1}^{n+1} - T_{Hi,j}^{n+1}) - \frac{1}{R_{HP}}(T_{Hi,j}^{n+1} - T_{Pi+1,j}^{n+1})\right] + \frac{\Delta t}{2m_{HTFi,j}C_H}\left[\dot{m}_{HTF}C_H(T_{Hi,j-1}^{n} - T_{Hi,j}^{n}) - \frac{1}{R_{HP}}(T_{Hi,j}^{n} - T_{Pi+1,j}^{n})\right]$$

- Pipe node with HTF on its inner edge and solid on its outer edge ($Pipe_{HS}$):

$$T_{Pi,j}^{n+1} = T_{Pi,j}^{n} + \frac{\Delta t}{2m_{Pi,j}C_P}\left[\frac{1}{R_{HP}}(T_{Hi-1,j}^{n+1} - T_{Pi,j}^{n+1}) - \frac{1}{R_{PS}}(T_{Pi,j}^{n+1} - T_{Si+1,j}^{n+1})\right] + \frac{\Delta t}{2m_{Pi,j}C_P}\left[\frac{1}{R_{HP}}(T_{Hi-1,j}^{n} - T_{Pi,j}^{n}) - \frac{1}{R_{PS}}(T_{Pi,j}^{n} - T_{Si+1,j}^{n})\right]$$

- Pipe node with HTF on its inner edge and an annulus on its outer edge ($Pipe_{HA}$):

$$T_{Pi,j}^{n+1} = T_{Pi,j}^{n} + \frac{\Delta t}{2m_{Pi,j}C_P}\left[\frac{1}{R_{HP}}(T_{Hi-1,j}^{n+1} - T_{Pi,j}^{n+1}) - \frac{1}{R_{PA}}(T_{Pi,j}^{n+1} - T_{Ai+1,j}^{n+1})\right] + \frac{\Delta t}{2m_{Pi,j}C_P}\left[\frac{1}{R_{HP}}(T_{Hi-1,j}^{n} - T_{Pi,j}^{n}) - \frac{1}{R_{PA}}(T_{Pi,j}^{n} - T_{Ai+1,j}^{n})\right]$$

- Pipe node with HTF on its inner edge and liquid on its outer edge ($Pipe_{HL}$):

$$T_{Pi,j}^{n+1} = T_{Pi,j}^{n} + \frac{\Delta t}{2m_{Pi,j}C_P}\left[\frac{1}{R_{HP}}(T_{Hi-1,j}^{n+1} - T_{Pi,j}^{n+1}) - \frac{1}{R_{PL}}(T_{Pi,j}^{n+1} - T_{Li+1,j}^{n+1})\right] + \frac{\Delta t}{2m_{Pi,j}C_P}\left[\frac{1}{R_{HP}}(T_{Hi-1,j}^{n} - T_{Pi,j}^{n}) - \frac{1}{R_{PL}}(T_{Pi,j}^{n} - T_{Li+1,j}^{n})\right]$$

And using the Backwards Euler approximation:

- Solid PCM node with pipe on the interior edge and an annulus of liquid on the outer edge $Solid_{PA}$ ():

$$T_{Si,j}^{n+1} = T_{Si,j}^{n} + \frac{\Delta t}{m_{Si,j}C_S}\left[\frac{1}{R_{PS}}(T_{Pi-1,j}^{n} - T_{Si,j}^{n}) - \frac{1}{R_{SA}}(T_{Si,j}^{n} - T_{Ai+1,j}^{n})\right]$$

- Solid PCM node with a liquid annulus on the inner edge and a liquid annulus on the out edge ($Solid_{AA}$):

$$T_{Si,j}^{n+1} = T_{Si,j}^{n} + \frac{\Delta t}{m_{Si,j}C_S}\left[\frac{1}{R_{AS}}(T_{Ai-1,j}^{n} - T_{Si,j}^{n}) - \frac{1}{R_{SA}}(T_{Si,j}^{n} - T_{Ai+1,j}^{n})\right]$$

- Solid PCM node with a liquid annulus on the inner edge and a liquid node on the outer edge that extends to the adiabatic boundary ($Solid_{AL}$):

$$T_{Si,j}^{n+1} = T_{Si,j}^{n} + \frac{\Delta t}{m_{Si,j}C_S}\left[\frac{1}{R_{AS}}(T_{Ai-1,j}^{n} - T_{Si,j}^{n}) - \frac{1}{R_{SL}}(T_{Si,j}^{n} - T_{Li+1,j}^{n})\right]$$

- Solid PCM node with a pipe on the inner edge and a liquid node on the outer edge that extends to the adiabatic boundary ($Solid_{PL}$):

$$T_{Si,j}^{n+1} = T_{Si,j}^{n} + \frac{\Delta t}{m_{Si,j}C_S}\left[\frac{1}{R_{PS}}(T_{Pi-1,j}^{n} - T_{Si,j}^{n}) - \frac{1}{R_{SL}}(T_{Si,j}^{n} - T_{Li+1,j}^{n})\right]$$

- Solid PCM node with a liquid annulus on the inner edge and the boundary on its outer edge ($Solid_{AE}$):

$$T_{Si,j}^{n+1} = T_{Si,j}^{n} + \frac{\Delta t}{m_{Si,j}C_S}\left[\frac{1}{R_{AS}}(T_{Ai-1,j}^{n} - T_{Si,j}^{n}) - \dot{Q}_{loss}\right]$$

- Solid PCM node with a pipe on its inner edge and the boundary on its outer edge ($Solid_{PE}$):

$$T_{Si,j}^{n+1} = T_{Si,j}^{n} + \frac{\Delta t}{m_{Si,j}C_S}\left[\frac{1}{R_{AS}}(T_{Ai-1,j}^{n} - T_{Si,j}^{n}) - \dot{Q}_{loss}\right]$$

- Liquid PCM node with pipe on its inner boundary and the boundary on its outer edge ($Liquid_{PE}$):

$$T_{Li,j}^{n+1} = T_{Li,j}^{n} + \frac{\Delta t}{m_{Li,j}C_L}\left[\frac{1}{R_{PL}}(T_{Pi-1,j}^{n} - T_{Li,j}^{n}) - \dot{Q}_{loss}\right]$$

- Liquid PCM node with a solid node on its inner boundary and the boundary on its outer edge ($Liquid_{SE}$):

$$T_{Li,j}^{n+1} = T_{Li,j}^{n} + \frac{\Delta t}{m_{Li,j}C_L}\left[\frac{1}{R_{PL}}(T_{Pi-1,j}^{n} - T_{Li,j}^{n}) - \dot{Q}_{loss}\right]$$

- Annulus PCM node with the pipe on its inner edge and a solid node on its outer edge ($Annulus_{PS}$):

$$T_{Ai,j}^{n+1} = T_{Ai,j}^{n} + \frac{\Delta t}{m_{Ai,j}C_L}\left[\frac{1}{R_{PA}}(T_{Pi-1,j}^{n} - T_{Ai,j}^{n}) - \frac{1}{R_{AS}}(T_{Ai,j}^{n} - T_{Si+1,j}^{n})\right]$$

- Annulus PCM node with a solid node on its inner edge and a solid node on its outer edge ($Annulus_{SS}$):

$$T_{Ai,j}^{n+1} = T_{Ai,j}^{n} + \frac{\Delta t}{m_{Ai,j}C_L}\left[\frac{1}{R_{SA}}(T_{Si-1,j}^{n} - T_{Ai,j}^{n}) - \frac{1}{R_{AS}}(T_{Ai,j}^{n} - T_{Si+1,j}^{n})\right]$$

- HTF node with pipe on its outer edge (HTF_{HP}):

$$T_{Hi,j}^{n+1} = T_{Hi,j}^{n} + \frac{\Delta t}{m_{HTFi,j}C_H}\left[\dot{m}_{HTF}C_H(T_{Hi,j-1}^{n} - T_{Hi,j}^{n}) - \frac{1}{R_{HP}}(T_{Hi,j}^{n} - T_{Pi+1,j}^{n})\right]$$

- Pipe node with HTF on its inner edge and solid on its outer edge ($Pipe_{HS}$):

$$T_{Pi,j}^{n+1} = T_{Pi,j}^{n} + \frac{\Delta t}{m_{Pi,j}C_P}\left[\frac{1}{R_{HP}}(T_{Hi-1,j}^{n} - T_{Pi,j}^{n}) - \frac{1}{R_{PS}}(T_{Pi,j}^{n} - T_{Si+1,j}^{n})\right]$$

- Pipe node with HTF on its inner edge and an annulus on its outer edge ($Pipe_{HA}$):

$$T_{Pi,j}^{n+1} = T_{Pi,j}^{n} + \frac{\Delta t}{m_{Pi,j}C_P}\left[\frac{1}{R_{HP}}(T_{Hi-1,j}^{n} - T_{Pi,j}^{n}) - \frac{1}{R_{PA}}(T_{Pi,j}^{n} - T_{Ai+1,j}^{n})\right]$$

- Pipe node with HTF on its inner edge and liquid on its outer edge ($Pipe_{HL}$):

$$T_{Pi,j}^{n+1} = T_{Pi,j}^{n} + \frac{\Delta t}{m_{Pi,j}C_P}\left[\frac{1}{R_{HP}}(T_{Hi-1,j}^{n} - T_{Pi,j}^{n}) - \frac{1}{R_{PL}}(T_{Pi,j}^{n} - T_{Li+1,j}^{n})\right]$$

The model solves mass and energy balances around finite volumes that represent the different phases and physical elements in the system (i.e., heat transfer fluid, pipe and storage material). To address the rapid calculating time necessary for large set of annual runs, two solution schemes are present in the code. First, a backwards Euler is used for fast trials. Then a Crank-Nicolson scheme, 2nd order in time and in space, can be used for more precise runs. The solution method of choice is specified as a parameter by the user.

For each internal time step, the component generates a set of

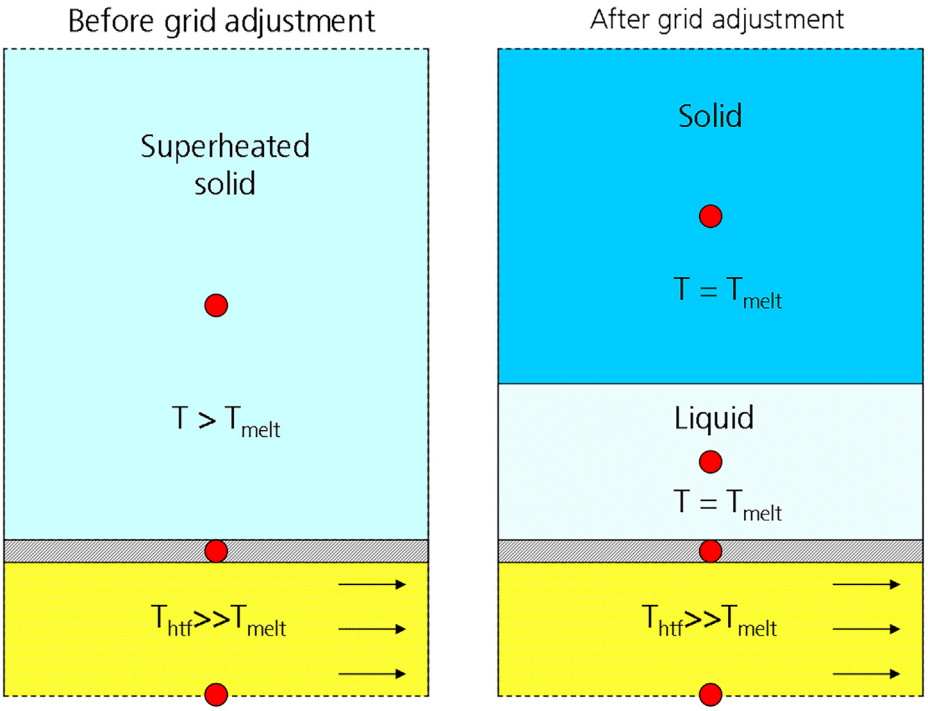

Fig. 5. The instantaneous adjustment of a melting axial slice of the PCM system.

matrices representing the governing equation of each node. The matrices are then solved using Gauss-Seidel iteration to find the temperatures for the next time step. If the new temperature is solid and above the melt point or liquid and below the melt point, the model adjusts the grid in order to accommodate the new state of the system. This grid adjustment process is described in Fig. 5 for a solid node above the melt temperature that needs to be adjusted into a solid node and a liquid node at the melt temperature.

The phase change process of each type of node is different, but the overall method followed is similar. A flow chart representation of the code being used can be found in Fig. 6.

The model has been validated running the model through different modes of operation and confirming compliance with thermodynamic laws. The focuses of each task were as follows:

1. Proving conservation of mass with both steady state and transient flow rate.
2. Proving conservation of energy with both steady state and transient flow rate and temperature.
3. Proving compliance with the second law of thermodynamics.
   - Given an artificially small convection loss terms, show that constant temperature is maintained in the tank when no filling or emptying is occurring.
   - Given an artificially large convection loss terms and artificially small specific heat for the salt, proving that the salt temperature approaches ambient temperature over time.

For each of these tasks the model was run and outputs were collected with the overall goal to expose any non-physical or unexpected system behaviour resulting from potential errors in the model (see Figs. 7 and 8).

Even though the authors agree with the reviewer that the models should be validated as much as possible, in this case this is not possible since there is no paper with the same or similar concept with experimental results. Moreover, the authors did not carry out an experimental campaign of this concept, since this is study is only a techno-economical evaluation of a new concept to assess its feasibility.

The model was subjected to a battery of test cases each designed to stress the code in a certain area. Overall the code showed conservation of energy within 1% and conservation of mass within 0.001%. These are typical values. The code can be setup to run with conservation of energy error less than 0.001%, but for computational runtime concerns this was not standard practice.

3.2. Plant modelling

Initially, the PCM model assumed the control strategy of the two tank system, considered the baseline in this study. However, once this basic control system was implemented the inherent complexities of the PCM system became more apparent. Nearly all of these complications arise from the transient nature of the heat transfer in a PCM system. After the first PCM runs with the controller used in the two tank baseline case, it became clear that more complex control options would be necessary to overcome several problems. These problems include: day-to-day repeatability, decaying outlet temperature during discharge, increasing outlet temperature during charge, and dissimilar charge and discharge pinch points. The complexities are mitigated through more complex control, including optimal field defocusing, night-time solidifications, power block re-route, and charging feed-water heater deactivation. Fig. 9 shows the complete TRNSYS project in the studio window. With the system built in this way annual performance modelling of any shell and tube based PCM system is possible.

3.3. Baseline case

The state-of-the-art TES technology, indirect two-tank molten salt [1], was chosen as the baseline for performance and economic comparison since its performance and cost are relatively established. A representative configuration of such a CSP plant with the baseline TES system is shown in Fig. 10.

More detailed specifications for the baseline plant are given in Table 2. The values calculated and comparisons made in this study are specific to storage capacity, assumed plant location, and all other plant specifications. A TES capacity of six equivalent full load hours (EFLH) of indirect storage was chosen as this is representative of systems currently in development. All performance and economic calculations

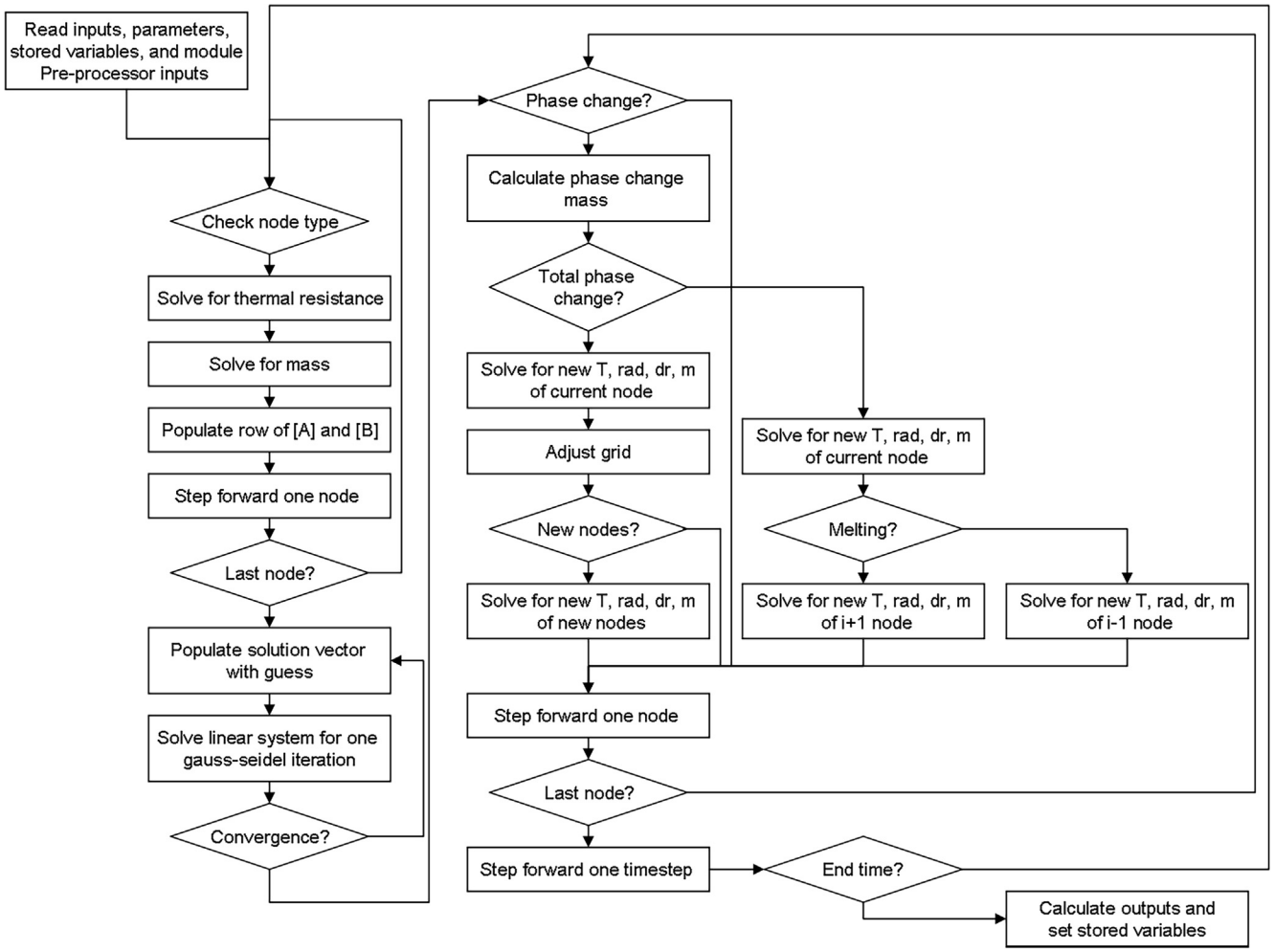

Fig. 6. TES model flow chart.

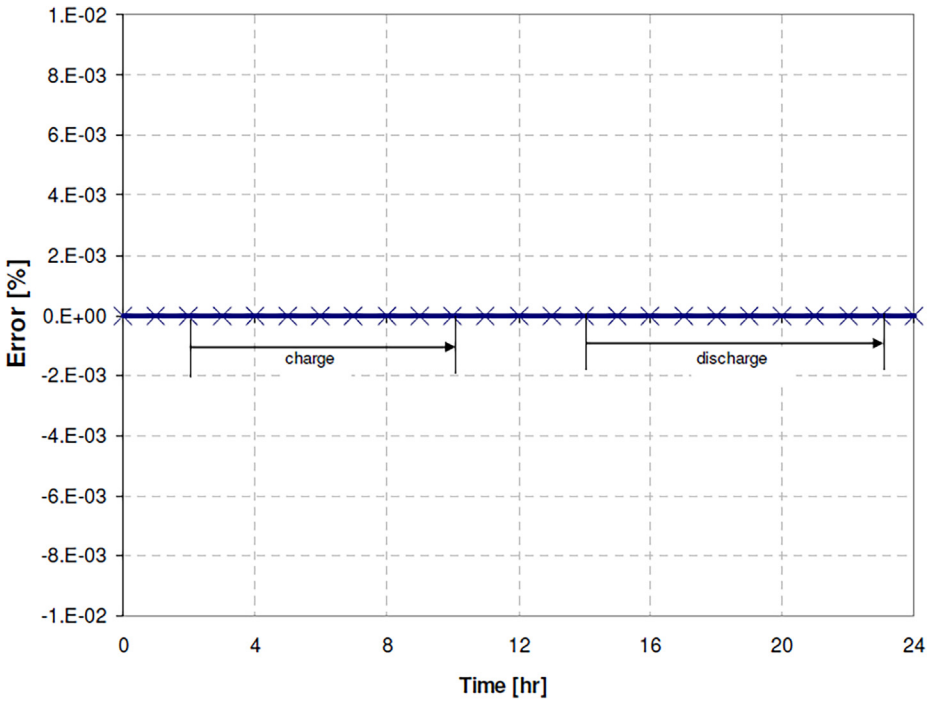

Fig. 7. Conservation of mass error during steady state and transient conditions.

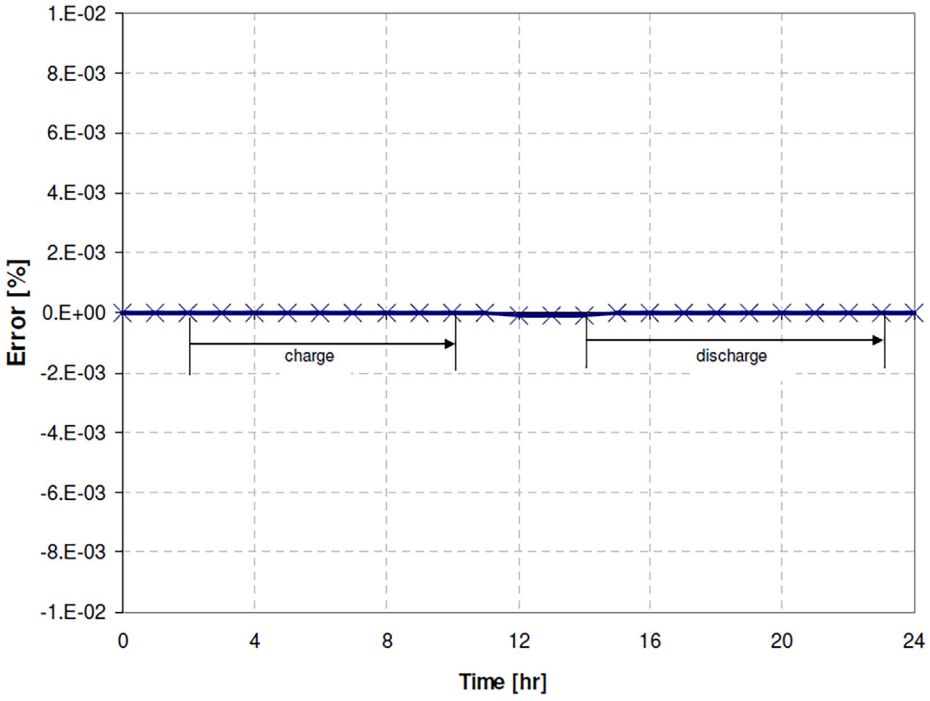

Fig. 8. Conservation of energy error during steady state and transient conditions.

assume the plant is located near Phoenix, AZ in the United States. The original size of the plant was intended to be 140 MW_{e_gross}, however, corrections to the power block performance model mid-project resulted in a 144 MW_{e_gross} turbine name plate capacity for the original component specifications.

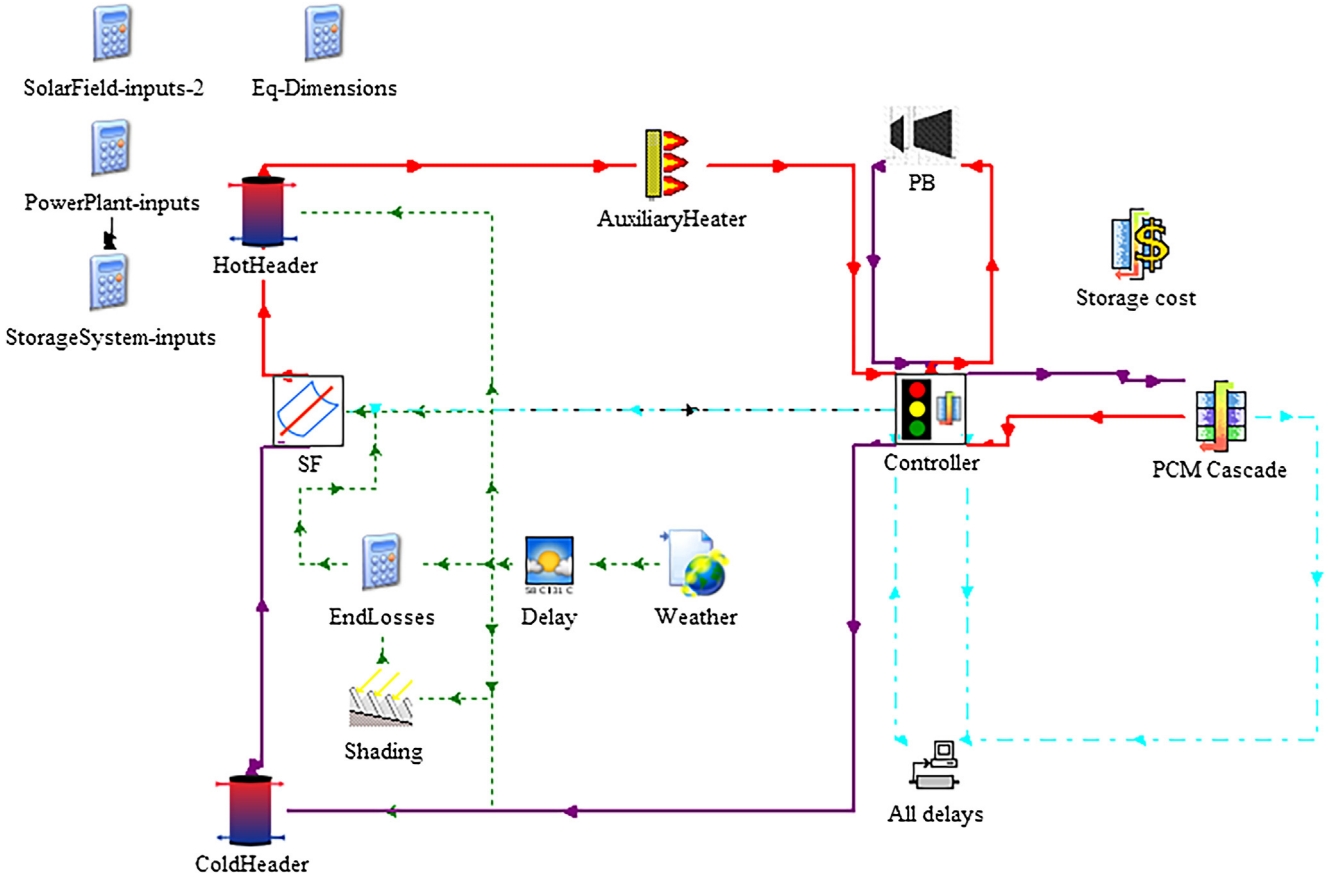

Fig. 9. TRNSYS Studio Project representation of the system code.

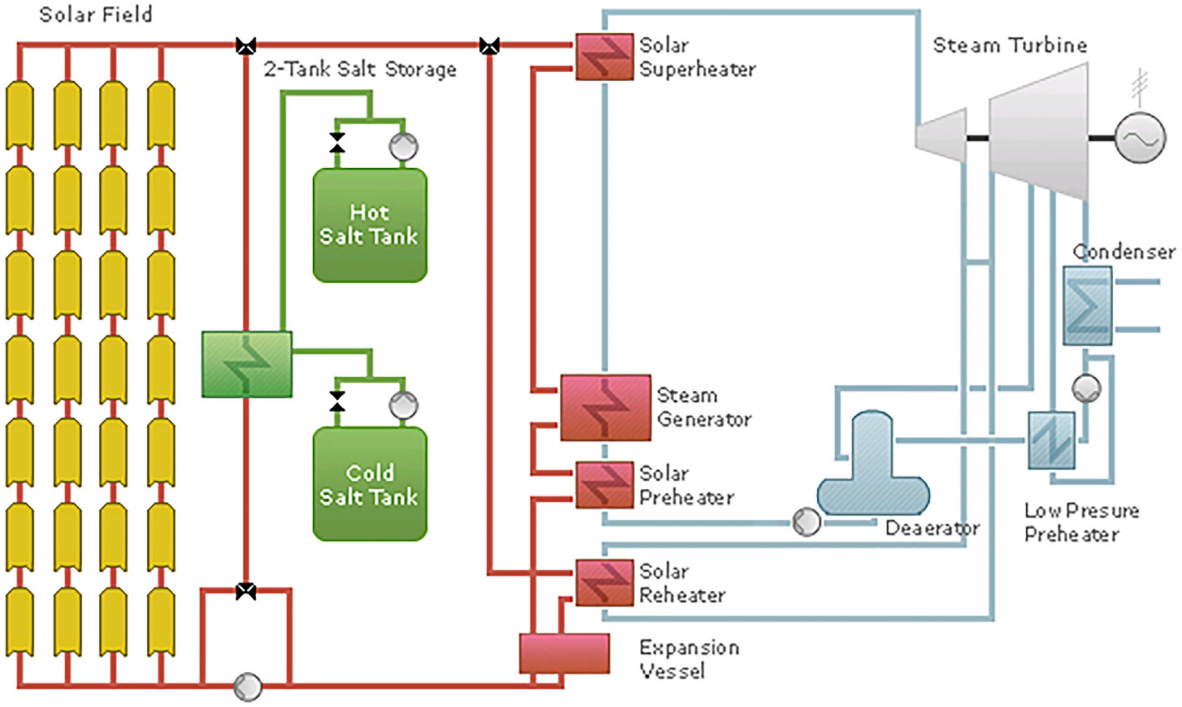

Fig. 10. Baseline plant configuration with indirect two-tank molten salt TES.

Table 2
Baseline CSP plant and TES specifications.

Component	Baseline
General	
Plant Location	Phoenix, AZ
Turbine Name Plate Capacity (gross)	144 MWe_gross
Plant Name Plate Capacity (net)	125 MWe_net
Solar Multiple	2.0
Power Block	
Power Cycle	Superheated steam Rankine cycle with reheat
Feed-water Heaters	5
Steam Inlet Pressure	100 bar (absolute)
Condenser Pressure	0.08 bar (absolute)
Steam Inlet/Reheat Temperature:	373.0/373.0 °C
Feed-water Temperature:	234 °C
Cooling	Wet
Solar Field	
Field Style	Parabolic Trough
Field Layout	"H" configuration
# of Loops	428
Module Aperture	5.76 m
Solar Field HTF	Therminol VP-1
Field Supply Temperature	393 °C (nominal)
Field Return Temperature	293 °C (nominal)
Thermal Energy Storage	
Storage Type	Indirect 2-tank molten salt
Storage Capacity	6 equivalent full load hours (864 MWh_{e_gross})
Number of Tanks	3 hot/3 cold
Storage Fluid	Binary salt (60% $NaNO_3$, 40% KNO_3)
Storage Fluid Quantity	66,613 metric tons
Hot Tank Temperature	386 °C
Cold Tank Temperature	295 °C

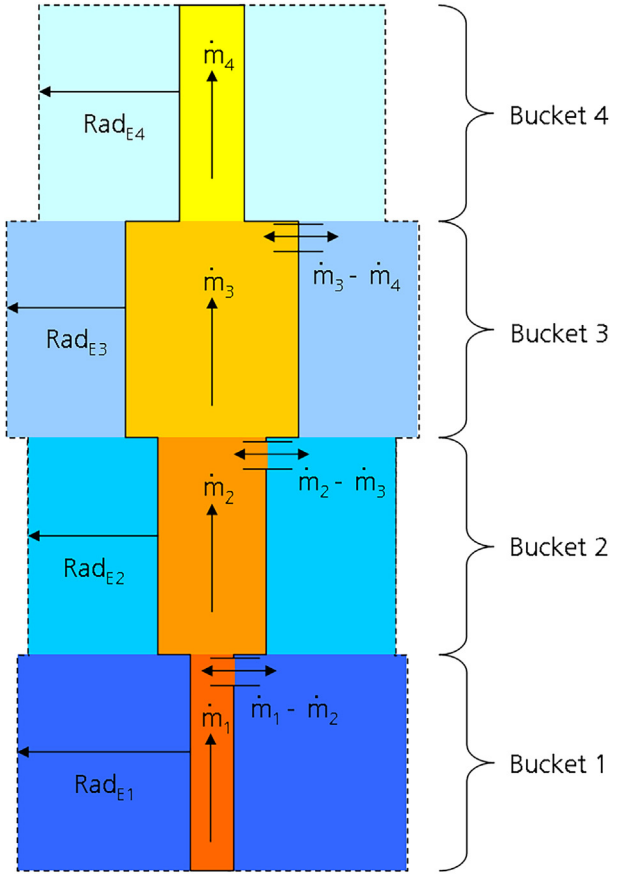

Fig. 11. Diagram of system as implemented in TRNSYS for ease of solving.

4. Results

4.1. Analysis of the PCM tanks performance

Since the model only considers one tube in the bucket and each bucket has a different number of tubes, the model must be able to solve for non-continuous mass flow throughout the system. Furthermore, each bucket may have a different radial spacing, set of material

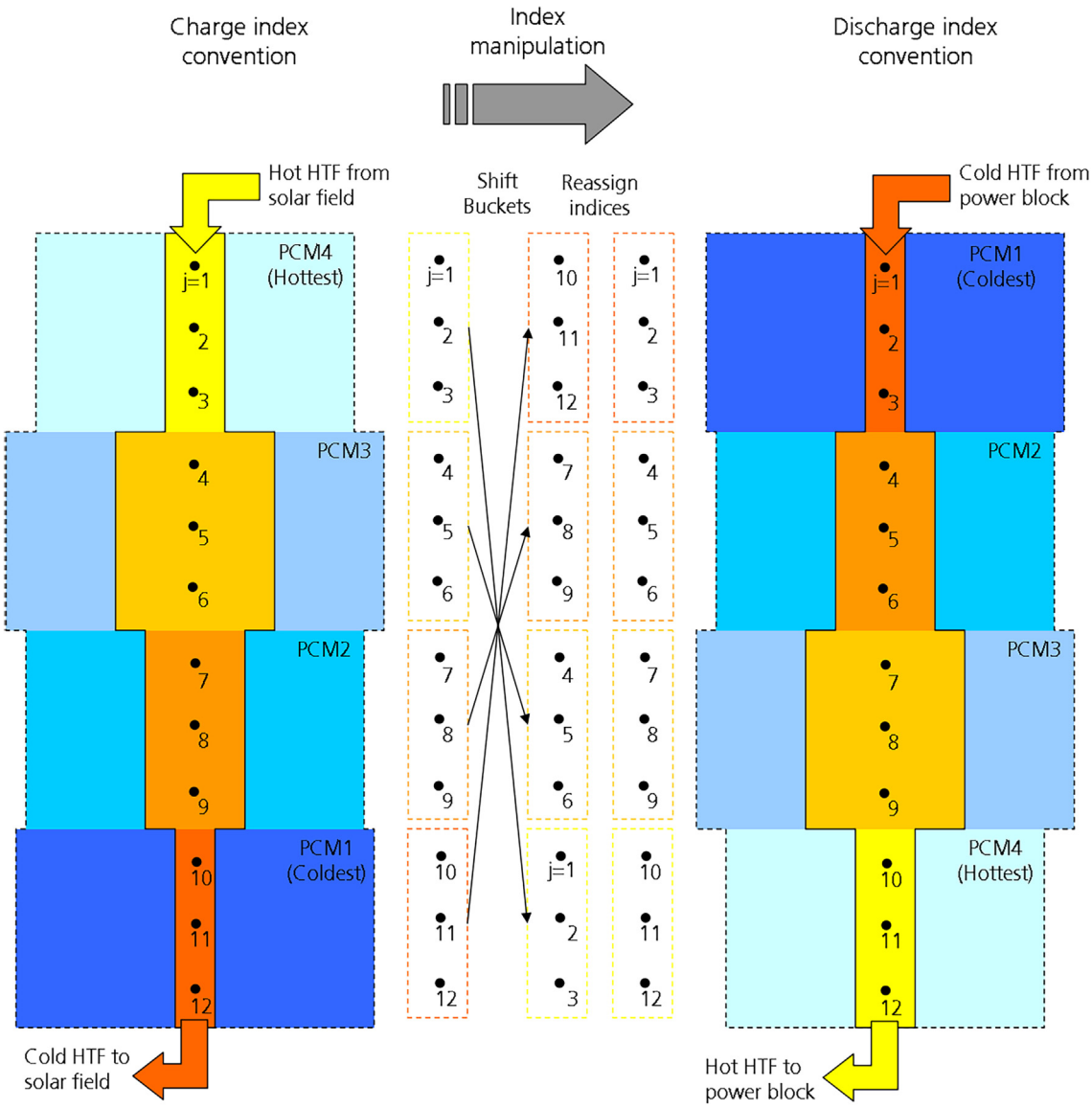

Fig. 12. Index manipulation methodology used for switching the system from charge to discharge.

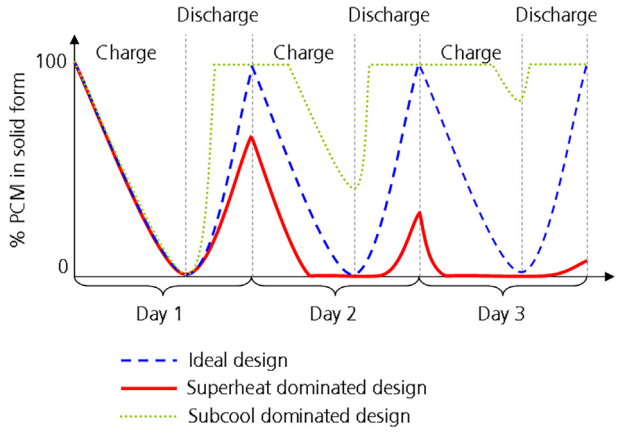

Fig. 13. Charge-discharge operation of the PCM TES systems with both an ideal and a poor day-to-day repeatable design.

properties, tube length, and tube diameter. Initially this appears complex, however, the implementation is somewhat simpler then the conceptualization.

Fig. 11 shows the system as implemented in TRNSYS. Conceptually the system is modeled as a single tube with various pipe and PCM radio. At the interface of each bucket the mass flow is uniformly and instantaneously changed to the mass flow for the next bucket. This change can be thought of as a valve with an entering or exiting mass flow equal to the difference between the mass flow of the current bucket and the mass flow of the next bucket in the cascade.

Fig. 12 shows the method used to adjust the indices of the system nodes. Because the physical system must always be run from the top down, the inlet of each bucket during charge and discharge is the same. However, during charge the hottest bucket is the first in the cascade and during discharge it is the last. When modelling the system as a single tube, the indices must be rearranged when switching from charge to discharge so that the buckets move but the internal indices of each bucket remain in the same order. This is done using the following equation, which solves for the new j index based on the system configurations and the current location in the system:

$$j_{new} = j - \frac{n_{pointsj}}{n_{PCM}}(n_{bucket} - 1) + n_{pointsj} - \frac{n_{pointsj}}{n_{PCM}}(n_{bucket})$$

where n_{bucket} is the bucket that the current node is in, $n_{pointsj}$ is the total number of axial slices in the system, and n_{PCM} is the number of PCMs in

Table 3
Average pinch points of the system encountered on May 25th.

Bucket	PCM	Melting temperature	Average charge pinch (°C)	Average discharge pinch (°C)	% difference
4	$MgCl_2$-KCl-NaCl	380	9.1	11.1	25%
3	NaOH-NaCl	371	12.3	15.4	7%
2	NaCl-KCl-LiCl	346	19.2	25.5	25%
1	$NaNO_3$ (coldest)	310	11.6	14.6	21%

Table 4
System dimensions varied in the parametrization to obtain the optimal system dimensions.

Dimension	Range	Units
Number to tubes	500–100,000	—
Extent radius	3.25–10.00	cm
Tube length	100–1000	m

Table 5
System dimensions after parametrization to obtain the optimal system dimensions.

Dimension	Bucket	Range	Units
Number to tubes	1	2500	—
	2	4000	
	3	4000	
	4	3000	
Extent radius	1	3.75	cm
	2	4.00	
	3	3.25	
	4	3.25	
Tube length	—	250	m

the cascade.

Day-to-day repeatability has, to our knowledge, never been investigated to any extent by other PCM research. The problem arises from the different driving temperature differences during charge and discharge combined with the tolerances of the outlet temperature and the variation in flow rates. For example, the third bucket, NaOH-NaCl, has a driving temperature difference of nearly 30 °C during charge compared to only a 10 °C temperature difference during discharge. Furthermore, the bucket sees a mass flow rate during charge that fluctuates between 0 and 1300 kg/s compared to a constant 1300 kg/s during discharge. On top of all this, the heat transfer characteristics are different for change and discharge for the salt. All of these factors combine to make the charging transient response of the system different to that of the discharging. This becomes a problem when attempting to design a system that will use 100% of the phase change material and yield the cheapest capital cost of the system. A system that is able to melt 100% of the PCM during charge may only be able to solidify 50% of the PCM during discharge. Then, the next day, it will melt the remaining 50% solid during charge and continue to superheat the PCM sensibly during the remainder of the charge. Now during discharge the system will only be able to solidify 25% of the PCM. This process will continue until only a small amount of the PCM is going through a phase change every day and the storage system has lost a significant portion of its storage density.

Fig. 13 shows the charge discharge behaviour of both an ideal PCM and two cases of poor day to day reliable PCM designs. Over time the subcool dominated system will exist exclusively as a solid and will only store heat sensibly, greatly reducing the effectiveness of the storage. The superheat dominated design will behave the same way, only storing heat sensibly in liquid. Of the three, only the ideal design will store heat in only the sensible range repeatedly for the life of the storage system.

Decaying outlet temperature during discharge was also added due to the need for increased control complexity. As the system solidifies the heat transfer is hindered by the increasing thermal resistance of the growing solid on the pipe. This leads to an outlet temperature that decays over time. A 350 °C outlet temperature tolerance was used as the cut-off point for when the PCM system would be considered empty. In some cases, this leads to large portions of some of the buckets never reaching 100% solid. This leads to poor TES performance. Furthermore,

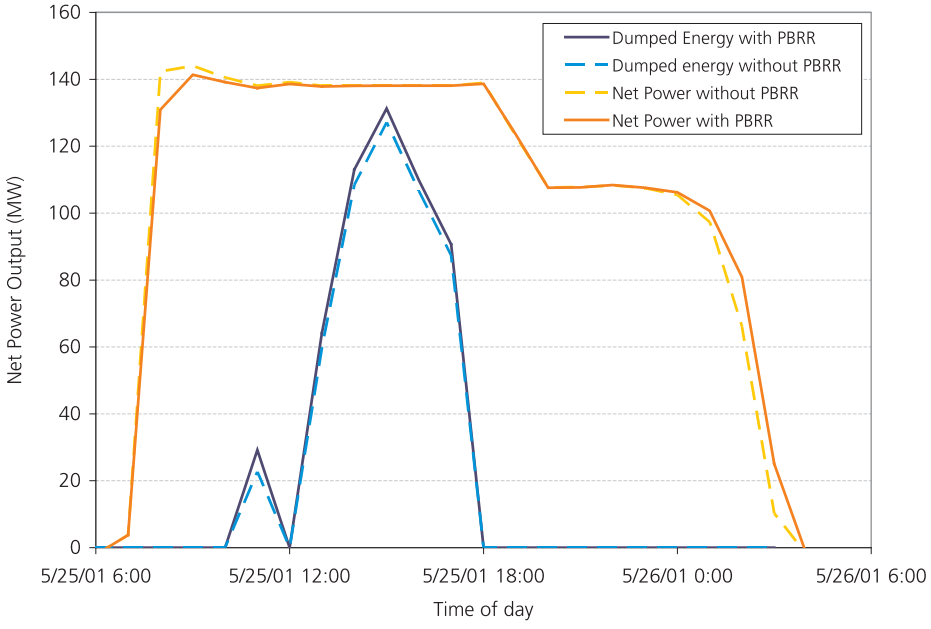

Fig. 14. Effect of the power block re-route on the PCM system.

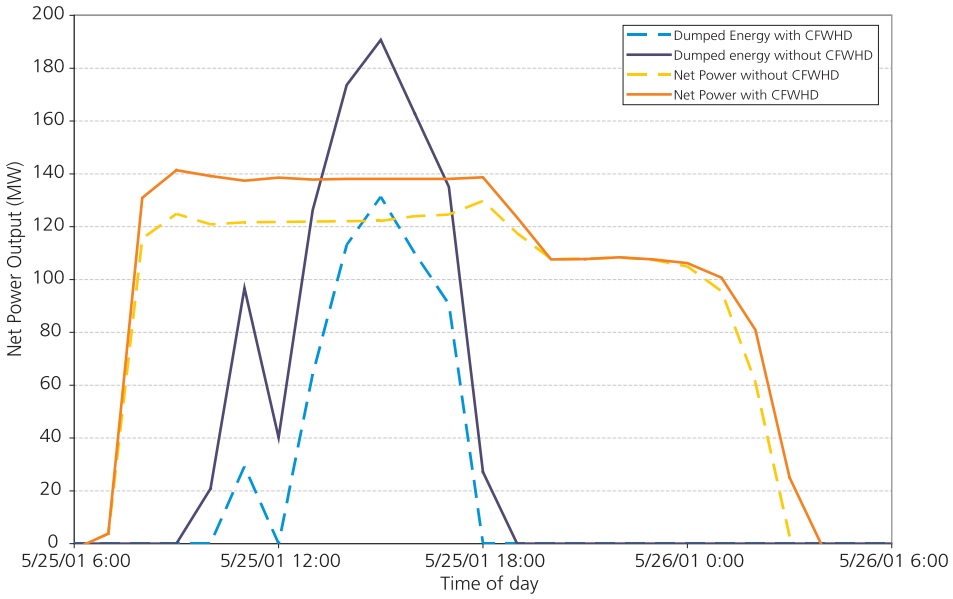

Fig. 15. Performance of the plant with identical system dimensions with and without charging feedwater heater deactivation.

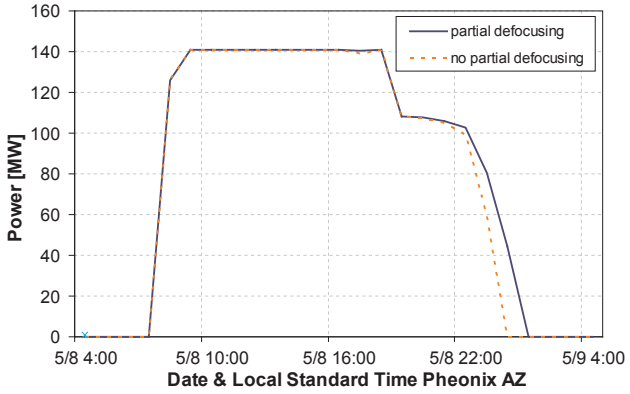

Fig. 16. Difference in plant performance when partial defocusing is used during charge.

this results in poor system utilization because the energy that was used to melt the PCM is not recovered if the PCM is not returned to 100% solid.

Similarly to decaying outlet temperature during discharge, the system is also affected by increasing outlet temperature during charge. As the system reaches 100% liquid and the PCM near the entrance of the tube is heated sensibly, the total driving temperature difference of the system is reduced and the outlet temperature increases. A tolerance of 330 °C for the inlet of the solar field was used to cap this outlet temperature increase. This cap creates a double edged problem. If, on one hand, the buckets are sized so that one bucket reaches 100% liquid before the others, the system will never reach holistically 100% liquid because the tolerance will be reached when the first bucket melts completely. Sizing in this manner leads to poor system utilization. On the other hand, an even bigger problem arises when the system is sized to reach holistically 100% liquid at the same time. A system sized in this manner will perform terribly during discharge with only one bucket

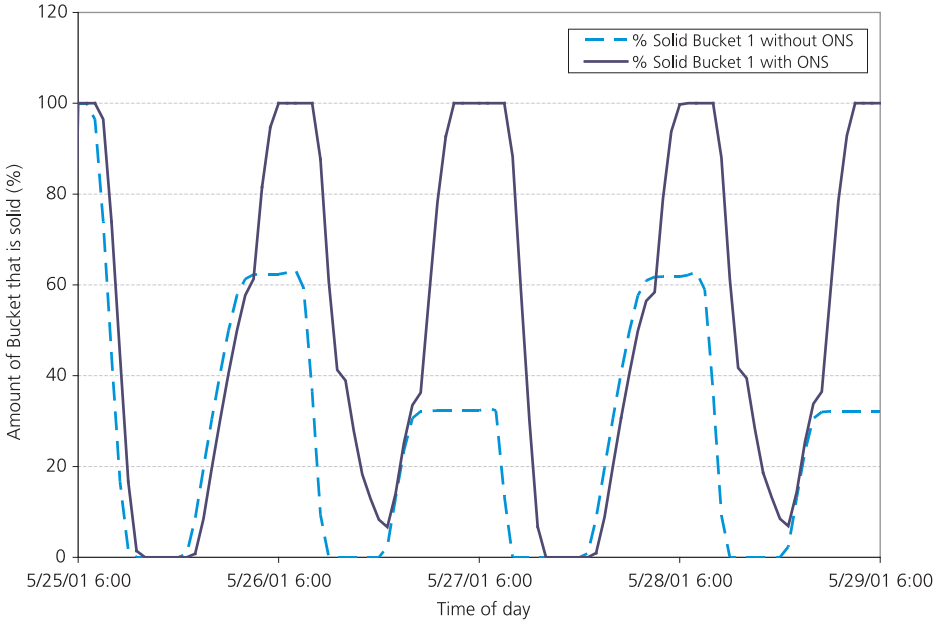

Fig. 17. Effect of the overnight solidification on the freeze-thaw cycle repeatability.

Table 6
System configuration of the power plant used to compare the PCM system to the Baseline.

Constant	Description	Value	Unit
$W_{turb,gross}$	Nameplate turbine capacity	144.1	MWe
t_{store}	Full load storage output time	6	hr
A_{col}	Collector area	861.16	m^2
n_{loops}	Number of loops in solar field	432	–
App_{col}	Collector aperture	5.76	m
$n_{col,loop}$	Number of collectors per loop	4	–
$m_{sf,design}$	Mass flow rate of solar field at design conditions	12,641,558	kg/h
$m_{st,min}$	Minimum mass flow rate of solar field	3,160,390	kg/h
avl_{sf}	Solar field availability	0.99	–
HTF	Heat transfer fluid used in the field	Therminol VP1	–
$m_{pb,design}$	Power block design mass flow rate	5,459,400	kg/h
$T_{setpoint,hot}$	Target hot temperature from solar field	393	°C
$T_{setpoint,cold}$	Target cold temperature from power block	311	°C
Location	Location of power plant	Phoenix, AZ	–

reaching 100% solid before the system must shut down due to the discharge temperature limits. This will lead to poor day to day reliability. Since the latter sizing problem has a much more dramatic effect on system performance, one must lean more towards a sizing paradigm that never fully reaches 100% liquid.

Theoretically, a cascaded system would have PCMs with melt points staggered so that each bucket melts at the same rate during charge and discharge. In reality, achieving equal rates is impossible because the melt points are not selectable, but rather are predetermined by the lattice structure of the PCM. This is further complicated by the fact that the pinch points are transient during charge and discharge.

Table 3 shows the pinch points encountered on May 25th during both charge and discharge. The main issue here is that the pinch points do not change equally for each bucket. Here bucket 3 experiences significantly less pinch point inflation during discharge. This leads bucket 3 to solidify at a slower pace than the other buckets unless a system sizing compromise is implemented. Overall, dissimilar charge/discharge pinch points lead to one of two things: either performance suffers due to pre-mature shutdown, or the utilization of the PCM must be compromised during charge so that the discharge performance is more similar between every bucket.

Initially, insufficient emphasis was put on proper system sizing. This led to systems with low day-to-day repeatability and performance. Eventually, it became clear that system dimensions were both critically important and unintuitive. Any bucket in the cascade is subject to two pinch point temperatures: the difference between the charge inlet HTF and the melt point and the difference between the discharge inlet HTF and the melt point. Furthermore, the thermal performance of each bucket is based on that PCM's thermal conductivity, enthalpy of fusion, and other thermal properties. This leads to a system with no intuitive or closed form, sizing method. Instead, a parametric sizing methodology has been adopted. Using GenOpt, a code developed by Laurence Berkeley National Lab, to run large optimizations, many thousands of system dimensions were tested and the best were selected. Table 4 shows the variables and ranges studied under this methodology and Table 5 the results of the parametrization.

Power block re-route is used to mitigate the decaying HTF outlet temperature from the TES system during discharge. Due to its small charge pinch point temperature, the quick depletion of the energy in the hottest bucket forces the PCM system to shut off prematurely. Using power block re-route, a portion of the HTF flowing to the power block is re-routed through just the hottest PCM bucket. This decreases the inlet temperature into the power block, but allows for more complete discharge of the entire storage system. Overall, there is a net energy gain when this control decision is implemented.

Fig. 14 shows the effect of power block re-route on the system. The configuration pictured uses 20% re-routed, meaning that only 20% of the HTF flow bound for the power block is run through the hottest bucket. This value was determined parametrically and will be re-determined for any new system. Furthermore, the number of tubes in the hot bucket can be increased or kept constant as the amount of re-route is varied. This parameter must also be parametrically derived for each new system.

Charging feedwater heater deactivation is a power block control modification that allows for more complete charging. Fig. 15 shows that during charge, the TES outlet temperature rises leading to higher inlet temperatures to the solar field, premature shutoff of the PCM storage charge cycle, and poor repeatable charging. By deactivating, or bypassing, some of the power block feedwater heaters during charging, the power block outlet temperature drops, compensating for the higher outlet TES temperature and allowing for more complete charging. This complete charging captures more energy than that lost by the lower efficiency of the power block and the result is a net increase in electrical

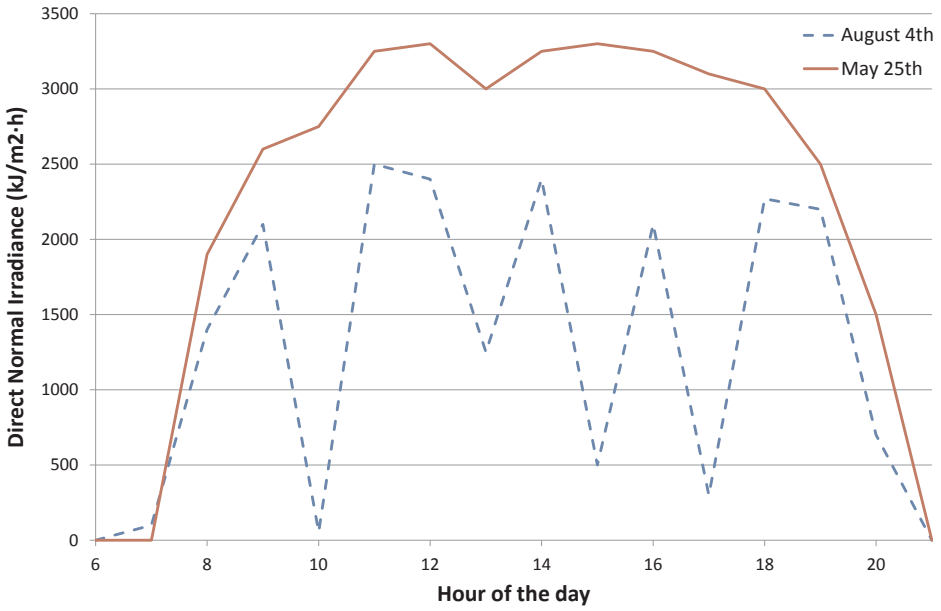

Fig. 18. Insolation for both May 25th and August 4th.

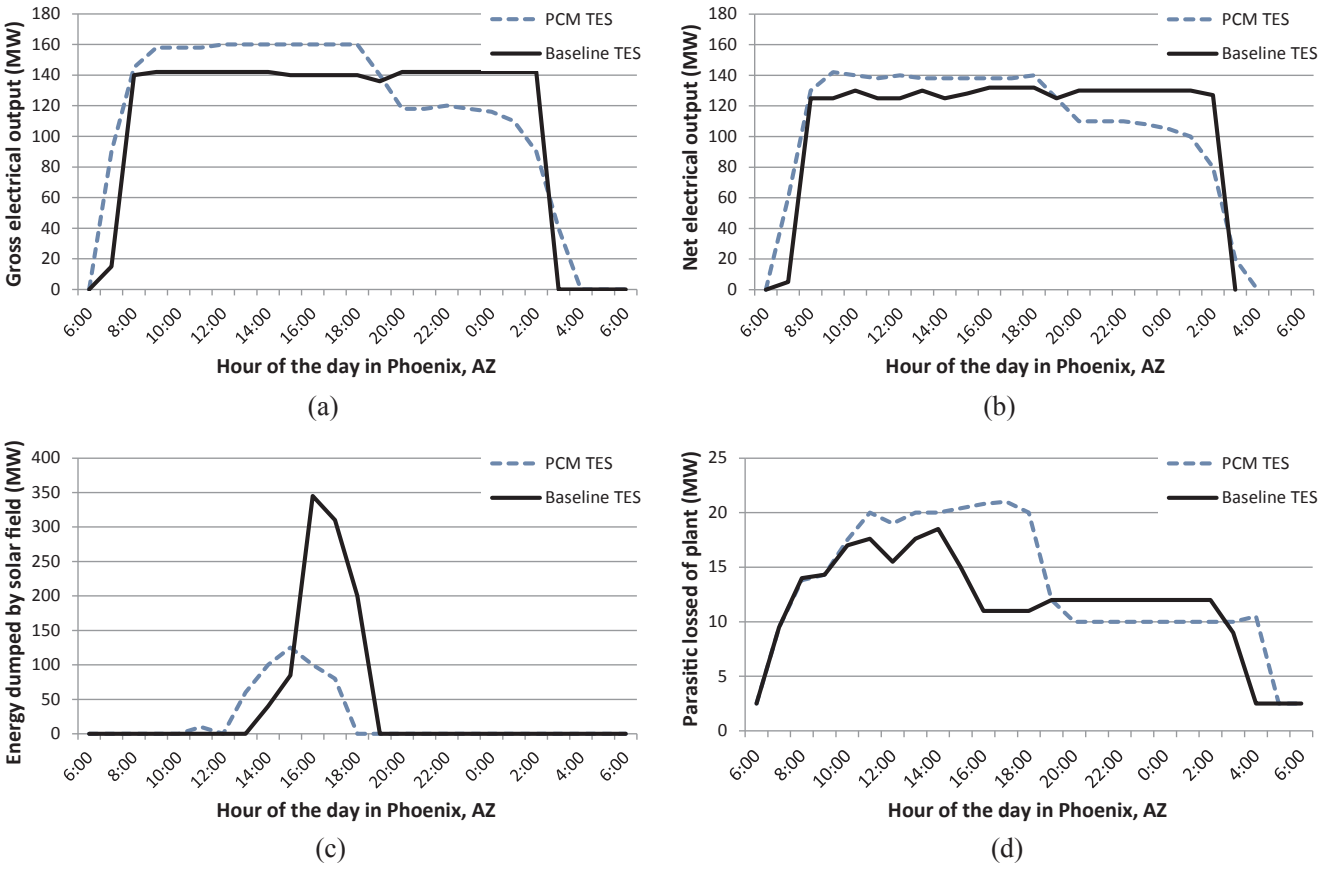

Fig. 19. Results of a "good" day, May 25th: (a) Gross electrical output, (b) net electrical output, (c) dumped energy, and (d) parasitic losses.

Table 7
TES efficiency and utilization for both systems on a representative "good" day May 25th.

Storage system	TES efficiency	TES utilization
Baseline TES	99.2%	77.8%
PCM TES	92.9%	80.9%

output and performance stability.

It is hard to capture in the comparison of net power the trade-off that the plant is being subjected to. Although the power output of the turbine is higher, its efficiency is lower. However, this is overcome by the significant reduction (up to 60%) in dumped energy due to the lower solar field inlet temperature, as shown in Fig. 15. Thus, the net production over the day is higher even though the system is being operated at a lower overall efficiency.

Another strategy is optimal solar field defocusing. Partial solar field defocusing allows for the energy input from the solar field to be decreased at times when the HTF temperature output of the storage gets too high to send back into the field. This lengthens the time the TES system can be charged during the day. The method for decreasing the energy input from the solar field is defocusing. Much like how the solar field provides just enough energy to fill the storage in the last time step of charge for the two tank system, the solar field is partially defocused so that it can accept a higher inlet temperature and operate at a lower mass flow to allow the TES outlet temperature to be near the design hot HTF. If the field is partially defocused, it can be fed a lower mass flow rate and a higher inlet temperature and still output the design hot HTF temperature. This reduced mass flow rate means that less energy is being captured by the field, since some of the mirrors that would be focusing extra light onto the absorber tubes are defocused.

Because the PCM model is not able to back calculate the ideal mass flow that would yield a solar field inlet temperature under the tolerance, an iterative calculation method is employed. First the plant is run as though it can store any mass flow rate the field provides. If the outlet temperature is too high after this iteration, then the controller decreases the overall solar field mass flow rate by 10% and another iteration is tried. This lower mass flow will allow more energy to be transferred into the TES system, shrinking the pinch point and decreasing the inlet temperature of the solar field. The controller will iteratively decrease the solar field mass flow rate until either the outlet temperature from the TES system is acceptable, or the minimum steam generator mass flow rate (500,000 kg/h) is reached. The next time step the controller will start again at 100% mass flow. This is so that, as the solar insolation decreases during the day, any spare energy will have a chance to be placed into storage. Fig. 16 shows the difference in plant performance for a system with and without partial defocusing. Although the increased performance appears slight on this graph, the increase in cost of the system is zero.

Overnight solidification takes advantage of the thermal losses from the field in order to solidify each bucket fully and increase the day-to-day repeatability of the system. Under the standard control regime, overnight freeze protection is provided by recirculation of the HTF through the field any time the power block is not being run. This leads to a slow degradation of the HTF temperature throughout the night. Instead, night time solidification uses constant HTF recirculation through the TES system in addition to the solar field. It includes the TES system in the recirculation until each bucket it solidified. To accomplish this, it solidifies the buckets one at a time until each is solidified. If the controller were to solidify each bucket at the same time the HTF would assume the hottest temperature and might melt the lower melt temperature buckets while the higher melt temperature buckets were being solidified. Similarly, to the weather prediction control strategy,

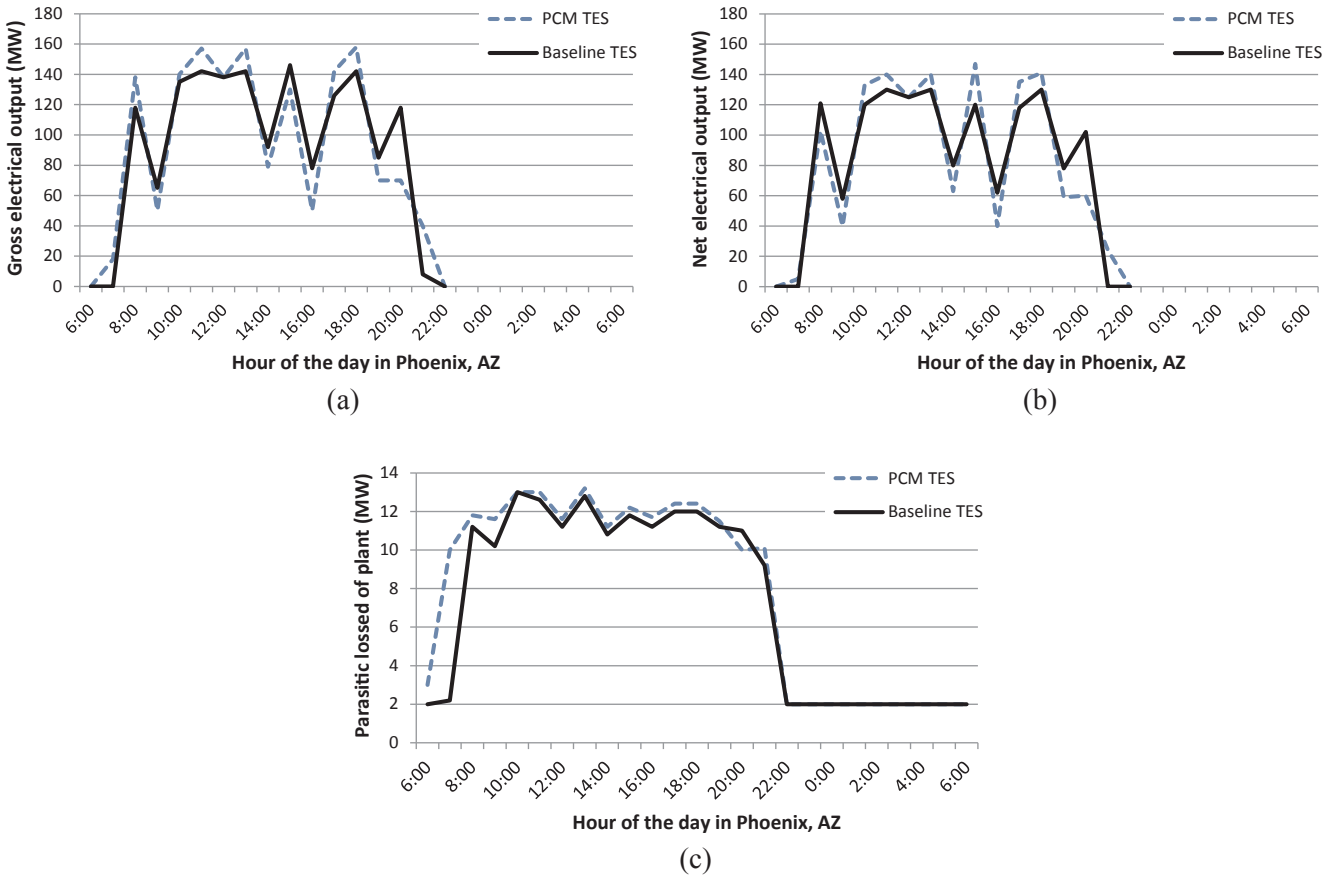

Fig. 20. Results of a "bad" day, August 4th: (a) Gross electrical output, (b) net electrical output, and (c) parasitic losses.

overnight solidification helps the system reset to a stable condition. Furthermore, overnight solidification reduces the need for warm-up time for the HTF in the solar field in the morning. However, it does increase the heat losses during the night and overall more energy is lost from the storage than we regain during warm-up. This is counteracted by the increase to day-to-day repeatability that is gained from overnight solidification. Fig. 17 shows the effect of the overnight solidification on the freeze thaw repeatability. Although only four days of operation are shown, the effect on repeatability is visible. Although this control change does not affect power output significantly over a single day, its long term effect is critical to the repeatable operation of the storage system.

4.2. Analysis of the performance of the TES integration in the CSP plant

Annual performance modelling is critical to the assessment of PCM as a TES option. Single charge discharge cycle modelling is not an acceptable means of measuring the performance of any TES system. For PCM systems this is especially true; their transient nature leads to system performance that can evolve over days or weeks and may never reach a steady state.

The TES system is not isolated from the plant. Its performance is directly linked to that of the solar field, the power block, and the main plant control strategy. Furthermore, the transient performance of the TES system changes the steady state operation of the power plant. If you have any transient in the TES system, it will affect the conditions in the HTF during the charge and the discharge, affecting the performance in the solar field and power block. Where an isolated model might assume a constant inlet temperature into the TES system during discharge, a full plant model will solve for the transient inlet temperature that exists for PCM systems.

Consequently, a fully integrated, transient power plant model was necessary to reach the goals of this paper. As described above, this model was created and implemented in TRNSYS. It was used to complete, daily, monthly, and annual simulations of plant performance for a CSP plant with a PCM storage system. Table 6 shows the system configurations that were used in both the PCM and baseline plants. The two plants were setup with the same system specifications outside of the TES system and the controller to allow for the most meaningful comparison.

Although the long term performance of the system is critical for the overall assessment of PCM TES, zooming into a single day is also insightful. Modelling was completed on a daily level for a representative "good" day, May 25th, and a "poor" day, August 4th. Fig. 18 shows the insolation values for both these days. This level of detail shows the inherent differences between the baseline and PCM systems. Most importantly it shows how the control strategies and intrinsic system properties impact the performance.

Fig. 19 shows the gross and net output of the system. The effects of charging feed-water heater deactivation is clearly visible in the PCM system as the turbine is made to run in an overpower mode during the charging hours of the day. In future phases of this project this overpower time will be reduced by implementing a control strategy that shifts this excess power to the storage system. This will mean a gross output closer to 140 MW during charging and a larger storage output. Also apparent is the transient nature of the PCM system. As the system moves from liquid to solid the effect on the performance is clearly evident. Also of interest on a daily basis are the dumped energy and parasitic losses of the system.

For the representative "good" day, the PCM plant performs similarly to the baseline. The main difference occurs in the overpowering of the turbine, the lower output during discharge, the reduced dumped energy

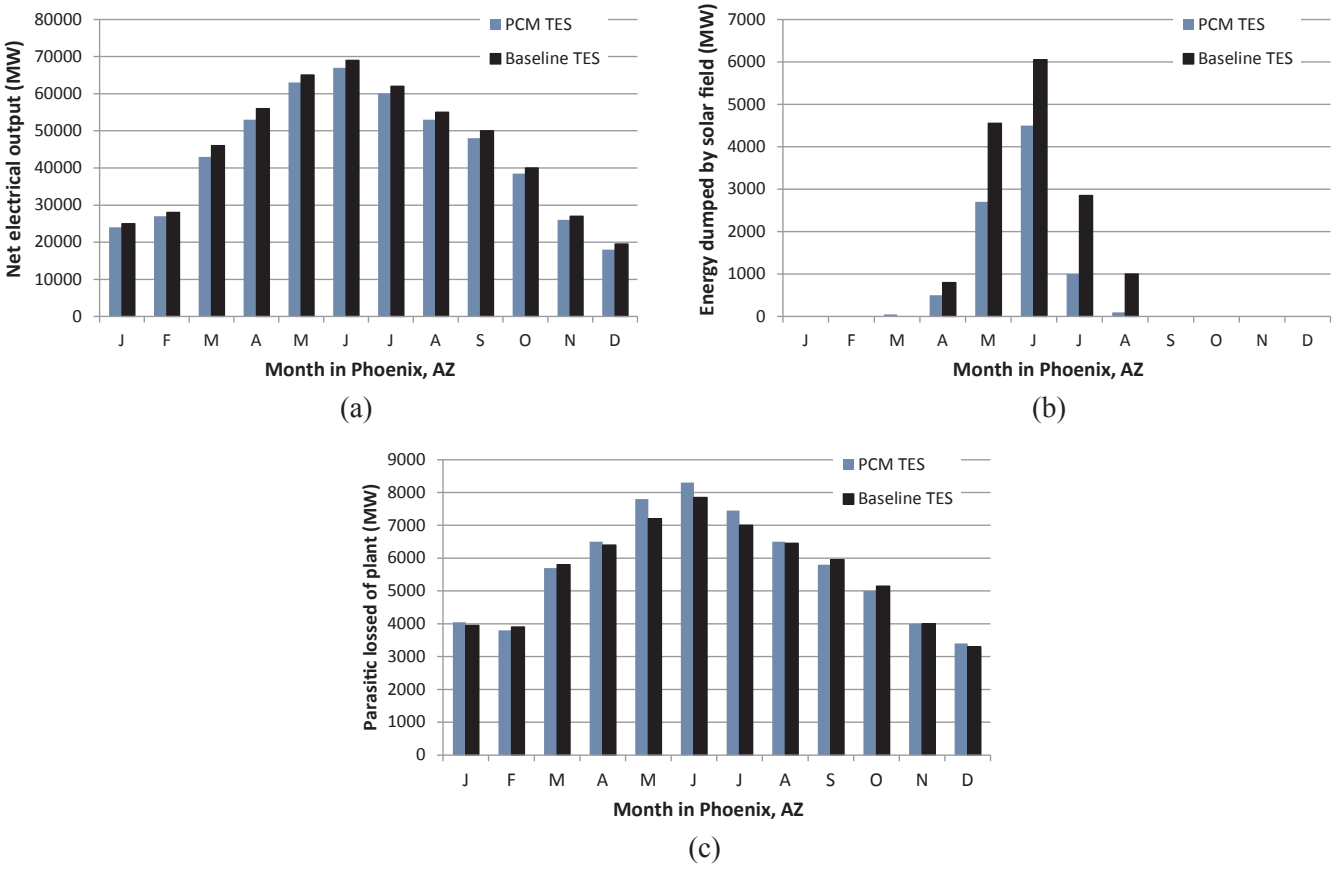

Fig. 21. Monthly results: (a) net electrical production, (b) energy dumped, and (c) parasitic losses.

and the higher parasitic losses. The lower output during discharge is largely due to the lower outlet temperature from the storage system then from the two tank system. The lower dumped energy is largely due to the low outlet temperature from the turbine during charge and the fact that the PCM system can be partially charge for the entirety of the day. The higher parasitic losses during charging result from the higher mass flow in the field necessitated by the solar field; allowing the PCM system to be charged for more of the day.

Using the same data, several values can be calculated that help compare the two systems. These are the TES utilization and efficiency. In general, they represent the amount the theoretical energy density that is used and the amount of energy that is recovered once it has been put into the storage system. PCM utilization is calculated using the equation below and represents the total energy stored in the storage system divided by the maximum potential energy that might be put into the storage system if the system was taken from the design outlet temperature of the plant, 293 °C, to the design solar field outlet temperature, 393 °C:

$$Utilization = 100\frac{\int_{discharge} \dot{m}_{htf}\, cp_{htf}\,(T_{TESout} - T_{PBout})}{\sum_{i=1}^{nPCM} (C_{pcm,i} m_{pcm,i}(T_{PBout} - T_{SFout}) + h_{f,i} m_{pcm,i})}$$

On the other hand, TES efficiency is the amount of energy retrieved from the storage divided by the amount of energy put into the system:

$$\eta_{TES} = 100\frac{\int_{discharge} \dot{m}_{htf}\, cp_{htf}\,(T_{TESout} - T_{PBout})}{\int_{charge} \dot{m}_{htf}\, cp_{htf}\,(T_{sfout} - T_{TESout})}$$

Table 7 shows these two values for the representative good day, May 25th.

In addition to the representative good day, May 25th, it was also important to look at a poor insolation day. August 4th was chosen as this day because it has low and highly transient insolation. Fig. 20 shows the gross, net, and parasitic performance of both systems for this day. Dumped energy is omitted because neither system has to de-focus the solar field on this day.

Monthly modelling is of interest to see the diurnal effects on both systems. It may be that some systems perform relatively better in winter or summer. Or, the performance of some system might be relatively better during the more transient fall or summer. Fig. 21 gives the net energy production, dumped energy and parasitic losses for each month. Overall, these plots show that, relative to each other, the PCM system and TES system perform similarly during winter, summer, fall and spring.

Although daily and monthly modelling are important, annual time frames are of the most interest to technology assessment. This data set gives the performance of the plant at every hour of the year, and eventually leads to the capacity factor for the plant. This allows for cost metrics to be calculated levelized to production so that a fair comparison can be made between the two technologies. Fig. 22 shows the cumulative net production, dumped energy, and parasitic losses for both systems. The important trends of these plots are shown in the slop of the lines. In addition to the final values that the plots show, they also show when the systems are accumulating power, dumped energy, and parasitic losses most rapidly. The PCM system, for example, is largely done dumping energy by July where since the two-tanks system still dumps a considerable amount of energy until mid to late August.

Although these plots illuminate some differences between the technologies, the important result of annual modelling are best summarized in tabular form. Table 8 shows a summary of the important annual performance metrics for both the PCM and Baseline TES systems.

The modelling analysis discussed above highlights several key issues that differentiate the PCM system from the baseline. Most importantly, these results highlight the transient nature of the PCM system. On the

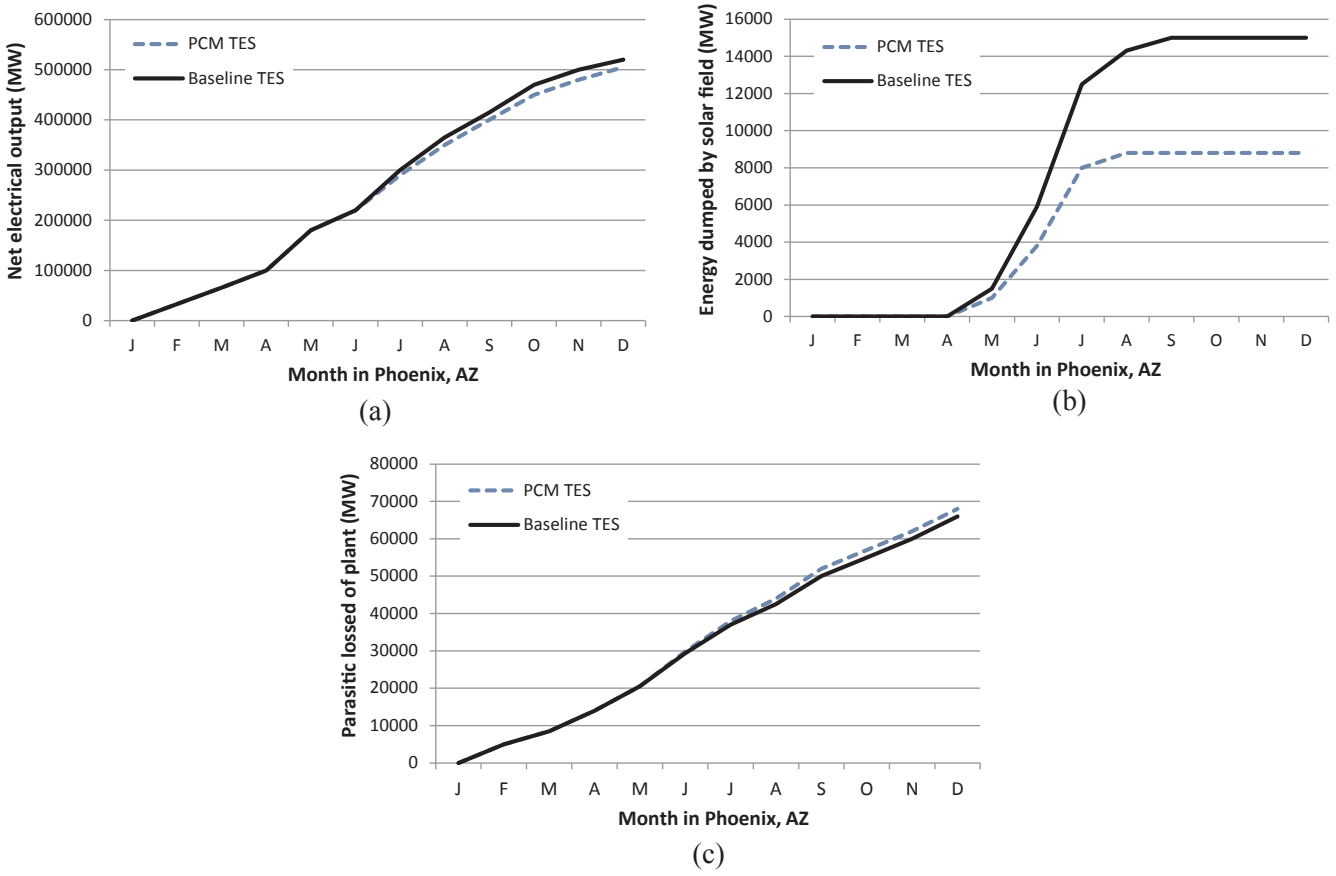

Fig. 22. Annual results: (a) net electrical output, (b) energy dumped, and (c) parasitic losses.

Table 8
Annual performance metrics of interest for both the PCM and Baseline system.

	PCM storage system	Baseline system	% difference
Gross electricity produced (MWh_e)	589,867	608,339	3.0%
Net electricity produced (MWh_e)	521,586	541,247	3.6%
Dumped energy (MWh)	8686	15,485	43.9%
Parasitic losses (MWh_e)	68,281	12,811	433%
Net electricity from storage (MWh_e)	115,271	155,298	25.8%
Capacity factor	47.63%	49.43%	3.6%
Efficiency	90.8%	98.2%	7.5%

daily plots this appears as the PCM output drops off near the end of the day. On the monthly and annual plot this appears as the consistent underperformance of the PCM system.

Also evident in this data is the superior performance of the PCM system where dumped energy in concerned. This is again due to the passive nature of the PCM system. Because the PCM system is very hard to "fill" it can keep absorbing some amount of energy far beyond the two tank system. On many days when the baseline system has to shut off its storage system and dump the additional energy from the solar field, the PCM system is capable of accepting a portion of the energy for the entirety of the day.

Another characteristic that is observed is the worse parasitic losses of the PCM system. The reasons for this are twofold: the PCM system runs more hours of the year then the Baseline, leading to higher pumping losses, and the PCM system runs at a higher mass flow during charge, leading again to higher pumping losses.

The final global takeaway from the system analysis is the similarity of the two technologies. Although the systems on a daily comparison appear different, the cumulative power production over the year is similar. As sized, both systems respond similarly to diurnal changes and, while aspects like the dumped energy seem dissimilar, overall the net production of both systems seems well matched.

5. Conclusions

This paper presents a technical assessment of the PCM energy storage systems used in solar thermal electricity plants. Performance analysis is conducted to evaluate the comparison of the PCM concept and two-tank molten salt thermal energy storage system for commercial parabolic through plant configuration.

The PCM thermal energy storage considered in this study utilizes an array of materials in four buckets ($NaNO_3$ in the first one; the mixture NaCl (33%) - KCl (24%) - LiCl (43%) in the second one; NaOH (80%) - NaCl (20%) in the third one; and the mixture $MgCl_2$ (60%) - KCl (20.4%) - NaCl (19.6%) in the fourth one) organized based on melting temperature and the latent energy change of materials to store thermal energy generated by the solar field.

A new model was developed to complete, daily, monthly, and annual simulations of plant performance, evaluating the transient performance of the PCM storage system integrated into a solar power plant

and estimating storage performance during a representative operation based on typical ambient conditions and solar radiation.

The modelling analysis highlight the transient nature of the PCM system, the superior performance of the PCM system where dumped energy in concerned and the worse parasitic losses of the PCM system.

The main conclusion from the system analysis is the similarity of the two technologies. The cumulative power production over the year is similar and the net production of both systems is well matched. Although this study confirms the technical feasibility of the PCM, a levelized cost metric comparison is needed to confirm the feasibility of the PCM as TES in commercial solar plant.

Acknowledgements

The work was partially funded by the Spanish government (ENE2015-64117-C5-1-R (MINECO/FEDER)). Dr. Cabeza would like to thank the Catalan Government for the quality accreditation given to her research group (2017 SGR 1537). GREiA is certified agent TECNIO in the category of technology developers from the Government of Catalonia.

References

[1] González-Roubaud E, Pérez-Osorio D, Prieto C. Review of commercial thermal energy storage in concentrated solar power plants: steam vs. molten salts. Renew Sustain Energy Rev 2017;80:133–48. https://doi.org/10.1016/j.rser.2017.05.084.

[2] Prieto C, Cooper P, Fernández AI, Cabeza LF. Review of technology: Thermochemical energy storage for concentrated solar power plants. Renew Sustain Energy Rev 2016;60:909–29. https://doi.org/10.1016/j.rser.2015.12.364.

[3] Muren R, Arias DA, Luptowski B. Performance based cost modeling of phase change thermal energy storage for high temperature concentrating solar power systems. ASME 2009 Int. Mech. Eng. Congr. Expo., ASME, Lake Buena Vista, Florida, USA. 2009. p. 193–202.

[4] Tamme R, Laing D, Steinmann W-D. Advanced thermal energy storage technology for parabolic trough. ASME 2003 Int. Sol. Energy Conf., ASME, Kohala Coast, Hawaii, USA. 2003. p. 563–71.

[5] Xu B, Li P, Chan C. Application of phase change materials for thermal energy storage in concentrated solar thermal power plants: a review to recent developments. Appl Energy 2015;160:286–307. https://doi.org/10.1016/j.apenergy.2015.09.016.

[6] Crespo A, Barreneche C, Ibarra M, Platzer W. Latent thermal energy storage for solar process heat applications at medium-high temperatures – A review. Sol Energy 2018. https://doi.org/10.1016/j.solener.2018.06.101.

[7] Belusko M, Tay NHS, Liu M, Bruno F. Effective tube-in-tank PCM thermal storage for CSP applications, Part 1: impact of tube configuration on discharging effectiveness. Sol Energy 2016;139:733–43. https://doi.org/10.1016/j.solener.2015.09.042.

[8] Belusko M, Tay NHS, Liu M, Bruno F. Effective tube-in-tank PCM thermal storage for CSP applications, Part 2: parametric assessment and impact of latent fraction. Sol Energy 2016;139:744–56. https://doi.org/10.1016/j.solener.2015.09.034.

[9] Abujas CR, Jové A, Prieto C, Gallas M, Cabeza LF. Performance comparison of a group of thermal conductivity enhancement methodology in phase change material for thermal storage application. Renew Energy 2016;97:434–43. https://doi.org/10.1016/j.renene.2016.06.003.

[10] Kumar A, Saha SK. Energy and exergy analyses of medium temperature latent heat thermal storage with high porosity metal matrix. Appl Therm Eng 2016;109:911–23. https://doi.org/10.1016/j.applthermaleng.2016.04.161.

[11] Galione PA, Pérez-Segarra CD, Rodríguez I, Torras S, Rigola J. Multi-layered solid-PCM thermocline thermal storage for CSP. Numerical evaluation of its application in a 50MWe plant. Sol Energy 2015;119:134–50.

[12] Abdulla A, Reddy KS. Comparative study of single and multi-layered packed-bed thermal energy storage systems for CSP plants. Appl Sol Energy 2017;53:276–86. https://doi.org/10.3103/S0003701X17030021.

[13] Elfeky KE, Ahmed N, Wang Q. Numerical comparison between single PCM and multi-stage PCM based high temperature thermal energy storage for CSP tower plants. Appl Therm Eng 2018;139:609–22. https://doi.org/10.1016/j.applthermaleng.2018.04.122.

[14] Wang J, Chen G, Jiang H. Theoretical study on a novel phase change process. Int J Energy Res 1999;23:287–94. https://doi.org/10.1002/(SICI)1099-114X(19990325)23:4<287::AID-ER476>3.0.CO;2-K.

[15] Peiró G, Gasia J, Miró L, Cabeza LF. Experimental evaluation at pilot plant scale of multiple PCMs (cascaded) vs. single PCM configuration for thermal energy storage. Renew Energy 2015;83:729–36. https://doi.org/10.1016/j.renene.2015.05.029.

[16] Mostafavi Tehrani SS, Shoraka Y, Nithyanandam K, Taylor RA. Cyclic performance of cascaded and multi-layered solid-PCM shell-and-tube thermal energy storage systems: A case study of the 19.9 MWeGemasolar CSP plant. Appl Energy 2018;228:240–53. https://doi.org/10.1016/j.apenergy.2018.06.084.

[17] Laing D, Bauer T, Lehmann D, Bahl C. Development of a thermal energy storage system for parabolic trough power plants with direct steam generation. J Sol Energy Eng Trans ASME 2010;132. https://doi.org/10.1115/1.4001472.

[18] Prieto C, Cabeza LF. Thermal energy storage (TES) with phase change materials (PCM) in solar power plants (CSP). Part 2 – Economic analysis, Appl Energy. (n.d.).

[19] Janz GJ, Allen CB, Bansal NP, Murphy RM, Tomkins RPT. Physical properties data compilations relevant to energy storage. II. Molten salts: data on single and multi-component salt systems; 1978.